HHS Public Access

Author manuscript

Clin Cancer Res. Author manuscript; available in PMC 2022 April 01.

Published in final edited form as:

Clin Cancer Res. 2021 October 01; 27(19): 5415–5429. doi:10.1158/1078-0432.CCR-20-5020.

PGC1α-Mediated Metabolic Reprogramming Drives the Stemness of Pancreatic Precursor Lesions

Rama Krishna Nimmakayala[1], **Sanchita Rauth**[1], **Ramakanth Chirravuri Venkata**[1], **Saravanakumar Marimuthu**[1], **Palanisamy Nallasamy**[1], **Raghupathy Vengoji**[1], **Subodh M. Lele**[2], **Satyanarayana Rachagani**[1], **Kavita Mallya**[1], **Mokenge P Malafa**[4], **Moorthy P. Ponnusamy**[1,3,*], **Surinder K. Batra**[1,3,*]

[1]Department of Biochemistry and Molecular Biology, College of Medicine, University of Nebraska Medical Center, Omaha, NE 68198-5870, USA

[2]Department of Pathology and Microbiology, College of Medicine, University of Nebraska Medical Center, Omaha, NE

[3]Eppley Institute for Research in Cancer and Allied Diseases, Fred & Pamela Buffett Cancer Center, University of Nebraska Medical Center, Omaha, NE

[4]Department of Gastrointestinal Oncology, H. Lee Moffitt Cancer Center and Research Institute, Tampa, FL, USA

Abstract

Purpose: Metabolic reprogramming and cancer stem cells (CSCs) drive the aggressiveness of pancreatic ductal adenocarcinoma (PDAC). However, the metabolic and stemness programs of pancreatic precursor lesions (PPLs), considered early PDAC development events, have not been thoroughly explored.

Experimental Design: Meta-analyses using gene expression profile data from NCBI GEO and immunohistochemistry on tissue microarrays (TMAs) were performed. The following animal and cellular models were used: cerulean-induced $Kras^{G12D}$; Pdx1 Cre (KC) acinar-to-ductal metaplasia (ADM) mice, $Kras^{G12D}$; $Smad4^{Loss}$; Pdx-1 Cre (KC^{Smad4-}) intraductal papillary mucinous neoplasm (IPMN) mice, LGKC1 cell line derived from the doxycycline-inducible Gnas IPMN model, and human IPMN organoids. Flow cytometry, Seahorse extracellular flux analyzer, qRT-PCR, and sphere assay were used to analyze metabolic and stemness features. SR18292 was used to inhibit PGC1α, and shRNA was used to knockdown (KD) PGC1α.

*Correspondence: Surinder K. Batra or Moorthy P. Ponnusamy, Department of Biochemistry and Molecular Biology, University of Nebraska Medical Center, Omaha, Nebraska, 68198-5870, USA Phone: 402-559-1170, Fax: 402-559-6650, sbatra@unmc.edu; mpalanim@unmc.edu.

Author contributions: SKB, MPP, and RKN conceived and designed the experiments. MPM provided materials; RKN performed the experiments. SR assisted with organoid culture; RC assisted with meta-analysis. SM, PN, KM, and RV assisted with in vitro experiments. SNR assisted with in vivo experiments. SKB, MPP, RKN, and SML analyzed the data. RKN wrote the manuscript. RKN, PPM, SKB, MPM reviewed and edited the manuscript.

Conflicts of interest

SKB is one of the co-founders of Sanguine Diagnostics and Therapeutics, Inc. The other authors disclosed no potential conflicts of interest.

Results: The meta-analysis revealed a significant upregulation of specific stemness genes in ADM-mediated pancreatic intraepithelial neoplasms (PanINs) and IPMN. Meta- and TMA analyses followed by *in vitro* and *in vivo* validation revealed that ADM/PanIN exhibit increased PGC1α and oxidative phosphorylation (OXPhos) but reduced CPT1A. IPMN showed elevated PGC1α, fatty acid β-oxidation (FAO) gene expression, and FAO-OXPhos. PGC1α was co-overexpressed with its coactivator NRF1 in ADM/PanINs and with PPARγ in IPMN. PGC1α KD or SR18292 inhibited the specific metabolic and stemness features of PPLs and repressed IPMN organoid growth.

Conclusions: ADM/PanINs and IPMNs show specific stemness signatures with unique metabolisms. Inhibition of PGC1α using SR18292 diminishes the specific stemness by targeting FAO-independent and FAO-dependent OXPhos of ADM/PanINs and IPMNs, respectively.

Keywords

PGC1α; pancreatic cancer; metabolic reprogramming; pancreatic precursor lesions

Introduction

Acinar-to-ductal metaplasia (ADM)-mediated pancreatic intraepithelial neoplasia (PanIN) (ADM-PanIN) and intraductal papillary mucinous neoplasm (IPMN) are the two significant pancreatic precursor lesions (PPLs) associated with PDAC prognoses (1). Distinct cell types in the pancreas respond differently to oncogenic insults. Recent evidence suggests that mutant Kras in pancreatic acinar cells induces ADM, a pre-precursor lesion that eventually develops into PanINs and PDAC (1). $Gnas^{R201C}$ mutation or the loss of Smad4 in the presence of $Kras^{G12D}$ activation results in IPMN (2,3). Recent genetic and histological analyses have shown evidence of the IPMN origin of PDAC (4). We have demonstrated previously that cigarette smoke-induced stemness is an early event in the oncogenic transformation of the pancreas (5). Though most of the studies refer to stemness as a cancer-initiating event (6–9), accurate stemness alterations and their regulation during PPL formation are unknown.

Altered metabolism in PDAC is the major factor impeding the treatment of PDAC (10). This metabolic reprogramming supports increased anabolism, leading to the elevated supply of building blocks necessary for the growth and survival of cancer cells. We and others have previously shown that a specific metabolic program regulates CSCs in tumors (11,12). However, the metabolic alterations that occur during PDAC initiation events and whether a specific metabolic program regulates stemness in PPLs are unknown.

In this study, data from both clinical samples and *in vivo* PPL models suggest that specific stemness and energy metabolic programs are elevated during the formation of ADM/PanINs and IPMNs. In particular, both lesions upregulate PGC1α, a central regulator of energy metabolism. Inhibition or KD of PGC1α repressed stemness by targeting FAO-independent and FAO-dependent OXPhos of ADM/PanINs and IPMNs, respectively, highlighting the role of PGC1α in PDAC initiation events.

Methods

Cell Culture and treatments.

Primary mouse cell lines, KC6141 and T161, were generated from the pancreas of genetically engineered mice $Kras^{G12D}$; Pdx-1 Cre (KC) and $Kras^{G12D}$; $Smad4^{Loss}$; Pdx-1 Cre (KC^{Smad4-}) mice, respectively. The LGKC1 primary cell line was derived from the doxycycline-inducible Gnas IPMN mouse model (p48-Cre; LSL-$Kras^{G12D}$; Rosa26R-LSL-rtTA-TetO-$Gnas^{R201C}$ mice or Kras; Gnas mice or KG mice). We received the LGKC1 primary cell lines as a kind gift from Dr. Anirban Maitra (MD Anderson). KC, KC^{Smad4-}, and LGKC1 cell lines were cultured in RPMI-1640 (Invitrogen Cat# 11875) supplemented with 10% FBS and 1% penicillin/streptomycin. Gnas was induced in LGKC1 cells by treatment with 10 ng-100 ng doxycycline. All cell lines were authenticated and verified as mycoplasma-free every month. In some experiments, cells were treated with vehicle control (DMSO) or SR18292 (Sigma Cat# SML2146), a selective inhibitor of PGC1α, at 40 μM for 48 hr. Human IPMN organoids were a kind gift from Dr. Mokenge Malafa, Moffitt Cancer Center, and were cultured as we did previously (13). Organoid growth after SR18292 treatment was monitored in the Incucyte Live-Cell Imaging analysis system (Essen BioScience).

Mouse treatment studies.

Animal experiments were carried out according to the UNMC Institutional Animal Care and Use Committee (IACUC) regulations. Mice were treated with cerulean (Sigma Cat# C9026) or PBS to induce acute pancreatitis as performed previously (14). Briefly, eight hourly intraperitoneal cerulean injections (75 μg/kg body weight) were given on two alternate days. The mice were sacrificed 2, 7, and 21 days after the last day of injection, and tissues were collected for analysis (Figure 1A).

Isolation of mouse primary pancreatic cells and 3D culture.

The pancreas was removed and washed with ice-cold HBSS media. The organ was minced into 1–5-mm pieces followed by digestion with collagenase P (HBSS media containing 10 mM HEPES, 0.5 mg/mL of collagenase P (Millipore Sigma Cat# COLLP-RO Roche), 10 μg/mL of DNase I, and 0.2 mg/ml of trypsin inhibitor (Thermofisher Scientific, Cat# 17075029). An equal volume of cold HBSS media containing 10% FBS was added after digestion to stop the digestion. The digested pancreatic pieces were washed twice with HBSS media containing 10% FBS and pipetted through a 100-μm cell strainer (Corning Cat# CLS431752). To make single cells, cells were incubated at 37°C for 5 min in trypsin. Cold HBSS media containing 10% FBS was added to stop the trypsin activity. Cells were washed and resuspended in HBSS media (containing 10 mM HEPES, 5% FBS, 10 μg/mL of DNase I, and 0.1 mg/ml trypsin inhibitor). For 3D culture, pancreatic cells were resuspended in a 1:3 media: Matrigel (growth-factor reduced, Corning, Cat# 354230). A 200 μl of suspension was seeded onto a 48-well plate and incubated for 30 min at 37°C to allow solidification. After solidification, we added 500 μl of RPMI medium supplemented with 10% FBS, 1% penicillin/streptomycin, 0.1 mg/mL soybean trypsin inhibitor, and indicated inhibitor. The number of duct-like structures were counted per field (whole well) after 5

days, and the images were captured using the EVOS FL Auto Imaging System (Thermo Fisher Scientific).

Generation of PGC1α stable knockdown cells.

The Colo357 pancreatic cancer cells with stable PGC1α knockdown (KD) and scrambled (SCR) control cells were generated using a PGC1α human shRNA plasmid kit (Origene, TG310260). LGKC1 cells with stable KD of PGC1α were generated using a mouse PGC1α shRNA plasmid (Santa Cruz, Cat# Sc-38885-SH) and control shRNA plasmid B (Sc-108065). Cells were transfected with SCR and shRNA plasmids using TurboFectin 8.0 transfection reagent (Origene, TF81001). 72 hr after transfection, GFP+-transfected Colo357 cells were sorted using FACS. Stably transfected cells were selected by treating with puromycin (2 μg/mL). The efficiency of PGC1α KD was examined using western blot and RT-PCR assays.

In vivo tumorigenicity assay.

Cells (15 million) were suspended in 500 μL PBS and mixed with Matrigel (Fisher Scientific) (1:1 ratio). Cells (1.5 million) in 100 μL were injected subcutaneously into the right and left flanks of 8-week-old athymic nude mice. Four to six mice were used per group, and the appearance of tumors was checked by palpation. Animals injected with LGKC1 cells were maintained with doxycycline in sucrose water. Animals were sacrificed soon after the tumor nodule reached a 1 to 1.5 cm diameter (after 3 weeks). Tumor size was assessed by external measurement of the tumors' length and width using a caliper as soon as tumors reached measurable size. The tumor volume was calculated using the formula: volume (mm^3) = 1/2 length (mm) × (width [mm])^2.

Sphere culture.

For sphere culture, cells were cultured in low-attachment culture plates in stem cell medium: DMEM/F12 (Invitrogen) supplemented with 1% B27, epidermal growth factor (20 ng/mL), and basic fibroblast growth factor (10 ng/mL). In some experiments, cells (2000/well or 500/well) were plated in 96-well low-attachment culture plates in 200 μL of the stem cell medium. The number of spheres for each well was monitored for 4 to 10 days. Images were captured using the EVOS FL Auto Imaging System (Thermo Fisher Scientific) or Incucyte Live-Cell Imaging analysis system (Essen BioScience). The number of spheres (>50 μm) was counted per field (whole well). In some experiments, sorted acino-ductal (AD) cells were seeded under sphere culture conditions and maintained in vehicle control (DMSO) or SR18292 (40 μM) for seven days before analysis.

Immunoprecipitation and immunoblotting:

Protein lysates (500 μg) were immunoprecipitated with 2 μl of rabbit anti-PGC1α (Invitrogen, Cat# PA5–72948) antibody. First, 20 μl of dynabeads (Invitrogen, Cat# 10004D) were incubated with rabbit anti-PGC1α antibody for 1 hr at room temperature. Afterward, protein lysates were incubated with the antibody-bound dynabeads overnight at 4°C. The next day, the immune complex on beads was washed three times with PBS, and the sample was eluted in 2X SDS-PAGE gel-loading buffer by heating the sample in a 95°C water

bath for 5 min. The immunoprecipitated products were subjected to 10% SDS-PAGE, then transferred onto a PVDF membrane and immunoblotted with mouse anti-PGC1α antibody 1:1000 (Santa Cruz Cat# 518025) and mouse anti-acetylated lysine antibody 1:1000 (Invitrogen, MA1–2021).

Western blotting analysis.

Cells were lysed in RIPA buffer (50 mM Tris-HCl, 150 mM NaCl, 1% NP-40, 0.5% sodium deoxycholate, 0.1% sodium dodecyl sulphate [SDS]) containing protease inhibitors (1 mM phenyl-methyl sulphonyl fluoride, 1 μg/ml aprotinin, 1 μg/ml leupeptin). Cell lysates were spun at 13,000 rpm for 30 min to remove debris, and protein quantification was performed using the Bio-Rad DC Protein Assay kit (RRID:SCR_008426). Total protein (40 μg/well) was fractionated by 10% SDS–PAGE. Fractionated proteins were transferred to polyvinylidene difluoride (PVDF) membranes. Membranes were blocked in 5% non-fat dry milk in PBS containing 0.1% Tween 20 (PBST). Blots were incubated overnight at 4°C with primary antibodies: ALDH1A1, 1:1000 (Santa Cruz Cat# Sc 374149), mouse anti-PGC1α, 1:1000 (Santa Cruz Cat# 518025) and Smad4, 1:1000 (RRID:AB_627905). β-actin was used as a loading control for protein normalization. The membranes were then washed in PBST, probed with the appropriate secondary antibodies, incubated for an hour at room temperature, and then washed with PBST. Signals were detected with the ECL chemiluminescence kit (Thermo Scientific).

Flow cytometry.

ALDH activity was measured using an AldeRed ALDH detection assay kit (EMD Millipore SCR150) following the manufacturer's instructions. Stained cells were analyzed using LSR II Green (BD Biosciences) with the green fluorescence channel (515–545 nm), and data were analyzed using the FACS DIVA software program (BD Biosciences). For sorting, single mouse primary acinar cells were incubated for 30 min with 100 μg/mL fluorescein isothiocyanate (FITC)-conjugated UEA-1 (Vector laboratories Cat# FL-1061–5) at room temperature in serum-free DMEM media (containing 0.1 mg/ml trypsin inhibitor and 10 μg/mL of DNase I). After washing, UEA1 FITC-labeled single acinar cells were stained with PE-Cy7 anti-mouse CD133 antibody (Biolegend 141209) in HBSS media (containing 10 mM HEPES, 5% FBS, 10 μg/mL of DNase I and 0.1 mg/ml trypsin inhibitor) for 20 min at 4°C. After washing, cells were stained with DAPI and analyzed/sorted using FACS Aria (BD Biosciences). In some experiments, acinar cells were stained with UEA1-FITC, AldeRed (Millipore, Cat# SCR150) or Super Bright 600 Anti-mouse cKit antibody (eBioscience, Cat# 63–1171-80), and PE-Cy7 anti-mouse CD133 antibody (Biolegend 141209).

Immunohistochemistry.

Tissue microarrays (TMAs), CP (US Biomax Cat# BIC14011b), and IPMN (CHTN_PanCA1) were purchased and subjected to immunohistochemical staining by using the following primary antibodies at the indicated dilution: PGC1α 1:100 (Santa Cruz Cat# 518025) and CPT1A 1:100 (Proteintech Cat# 15184-I-AP). Antigen retrieval was performed in 10 mM sodium citrate buffer (pH 6). The stained sections were scored by Dr. Subodh M. Lele (pathologist, UNMC). The intensity of protein expression was graded on a scale of

0 to 3 (0, no staining; 1+, weakly positive; 2+, moderately positive; 3+, strongly positive). The percentage of positive staining was scored in a range of (0–100% or 0–1). A histoscore was calculated by multiplying intensity (0–3) and positivity (0–1), ranging between 0 and 3. GraphPad Prism software (RRID:SCR_002798) was used to calculate *P* values and to design graphs.

Immunofluorescence staining.

Harvested tissues were fixed in 10% formalin and embedded in paraffin. Immunofluorescence analysis of tissue sections was performed as shown previously (11). Briefly, slides were baked for 2 hr at 60°C, deparaffinized in xylene, and rehydrated sequentially in ethanol. For antigen retrieval, slides were microwaved in sodium citrate buffer for 15 min. Slides were blocked in 5% normal goat serum and incubated with primary antibody overnight at 4°C. The primary antibodies used in this study include PGC1α 1:100 (Santa Cruz Cat# 518025), CPT1A 1:100 (Proteintech Cat# 15184-I-AP), Paf1 1:100 (developed in-house), CD133 1:100 (RRID:AB_470302), Smad4 1:100 (Santa Cruz Cat# sc7966), NRF1 1:300 (RRID:AB_2766328), anti-mouse c-Kit 1:100 (eBioscience, Cat# 11–1171-81), non-phospho active β-catenin 1:100 (Cell Signaling, Cat# 8814S), PPARG 1:100 (RRID:AB_10985650), and ALDH1A1 1:100 (RRID:AB_10917910). We also used conjugated lectins, UEA1-FITC, PNA-Rhodamine 1:100 (Vector Cat# RL-1072), and DBA-FITC 1:100 (Vector Cat# FL-1031). After washing in PBS, tissue slides were incubated with fluorophore-conjugated secondary antibody for 1 hr at room temperature. Slides were washed in PBS and mounted with Vectashield containing 4′,6-diamidino-2-phenylindole (DAPI). Whole-mount immunofluorescence staining for organoid cultures was performed as shown previously (15). Fluorescent images were captured using an LSM 710 confocal microscope and analyzed using ZEN software. For immunofluorescence on cells, we used Mitotracker Deep Red FM (Thermofisher Scientific Cat# M22426).

Quantitative PCR.

Total RNA was isolated using the RNeasy mini kit (Qiagen 74106) according to the manufacturer's instructions. Reverse transcription was performed from 2 μg of total RNA utilizing a SuperScript II cDNA synthesis kit (Invitrogen 18064–014). Quantitative PCR was performed using SYBR Green dye (Roche 04887352001) using a CFX Connect Real-Time PCR detection system (BioRad 1855200). Reactions were performed in triplicate, and β-actin was used as a control. Primers used are listed in Supplementary Table 1.

Seahorse extracellular flux analysis of ECAR and OCR.

Extracellular acidification rate (ECAR), oxygen consumption rate (OCR), and fatty acid-β oxidation OCR (FAO-OCR) were measured as we performed previously (11). Briefly, 10,000 cells were plated in XF96 cell culture microplates (Seahorse Biosciences, Cat# 101104–004) in the respective growth medium. After 24 hr, the growth medium was replaced with XF assay medium (Seahorse Biosciences, Cat# 102365–100) followed by incubation at 37°C for 1 hr in a CO_2-free incubator. The basal ECAR and the ECAR following the addition of glucose (10 mM), oligomycin (1 μM), and 2-deoxyglucose (50 mM) were measured using an XF96 extracellular flux analyzer (Seahorse Biosciences) by following the manufacturer's protocol. The ECAR values were normalized to total cell

counts in each well. The basal OCR and the OCR following the addition of oligomycin (1 μM), FCCP (0.5 μM), and rotenone/antimycin A (0.5 μM) were measured using an XF96 extracellular flux analyzer (Seahorse Biosciences) by following the manufacturer's protocol. The ECAR values were normalized to total cell counts in each well. FAO-OCR was measured by the XF Cell Mito Stress Test (Cat# 103015–100) using the XF Palmitate-BSA FAO substrate (Cat# 102720–100) in the presence or absence of etomoxir, an inhibitor of CPT1A, according to the manufacturer's instructions. The OCR values were normalized to total cell counts in each well.

Bioinformatics.

Two NCBI GEO datasets (GSE19650 and GSE43288) including clinical samples of the normal pancreas, intraductal papillary mucinous adenomas (IPMA or IPMN with low-grade dysplasia), intraductal papillary mucinous carcinomas (IPMC or IPMN with high-grade dysplasia), invasive ductal carcinomas (IDC) arising in IPMNs (IDC-IPMNs), PanINs, and PanIN-derived PDAC were selected to investigate the differential transcriptomic signatures of stemness and metabolic genes. The data were processed by quantile normalization and log2 transformation. Network analysis was performed by importing fold changes of differentially expressed genes (IPMN vs. NP or PanIN vs. NP) using Ingenuity pathway analysis (IPA) software (RRID:SCR_008653).

Statistical analysis.

Statistical analysis was performed using GraphPad Prism. Data are presented as the mean ± SD or mean ± SEM. Significance was determined using a simple student t-test and Dunnett's multiple comparisons test. Protein-protein interactions of PGC1α were analyzed using 'STRING" (https://string-db.org) (RRID:SCR_005223).

Results

A meta-analysis of metabolic and stemness genes in clinical samples of IPMN- and PanIN-mediated PDAC progression

We investigated the metabolic and stemness gene expression patterns of IPMNs and PanINs, using the gene expression profile data (GSE19650 and GSE43288) from the NCBI Gene Expression Omnibus (GEO) database. The GSE19650 dataset contains 7 samples of normal pancreas ducts (NP), 6 intraductal papillary mucinous adenomas (IPMA or IPMN with low-grade dysplasia), 6 intraductal papillary mucinous carcinomas (IPMC or IPMN with high-grade dysplasia), and 3 invasive ductal carcinomas (IDC) arising in IPMNs (IDC-IPMN or IPMN-PDAC). The GSE43288 dataset contains 20 samples, including 3 NP, 13 PanIN, and 4 PDAC (PanIN-derived PDAC or PanIN-PDAC) samples. Datasets were processed using standard GEO2R analysis, followed by quantile normalization and log2 transformation. The expression levels of genes encoding glycolytic and Warburg effect enzymes were not significantly elevated in IPMA, IPMC, and IPMN-PDAC samples compared with NP (Figure 1A–G). The expression levels of genes that encode oxidative phosphorylation (OXPhos) enzymes such as IDH1, MDH1, NDUFS2, and UQCRC1 were increased in different stages of IPMN compared to NP (Figure 1H–K). Interestingly, significant upregulation of PPARGC1A (PGC1α) and downregulation of cMyc were

observed in IPMA, IPMC, and IPMN-PDAC samples compared to NP (Figure 1L and M). Further, IPMC and IPMN-PDAC samples showed significantly higher expression of CPT2, a gene that encodes an enzyme that regulates the rate-limiting step of fatty acid β-oxidation (FAO) (Figure 1N). Glycolytic genes showed significantly elevated expressions in PanIN-derived PDAC; however, the expression of these genes did not vary substantially in PanINs compared with NP (Figure 1O–U). Unlike in IPMN, expression levels of PPARGC1A and FAO genes CPT1A and ACADS were not significantly different in PanINs and PanIN-derived PDAC compared with NP (Figure 1V–X). Overall, this metadata analysis suggests that IPMN samples exhibit a PGC1α/FAO-dependent OXPhos signature, while PanINs do not. Regarding stemness genes, IPMN and PanIN samples showed significantly elevated ($p<0.05$) expression levels of PROM1, ALDH2, LIF, NANOG, and KLF4. In addition, KIT, NOTCH2, and CD34 stemness genes were significantly and exclusively elevated in PanINs, while the expression levels of CTNNB1 and ALDH3A1 increased exclusively in IPMNs. (Figure 1Y and Supplementary Figure 1A and B). Ingenuity pathway analysis (IPA) of differentially expressed stemness and metabolic genes from the IPMN datasets followed by network generation showed an association of PGC1α with stemness, OXPhos, and FAO genes in IPMNs (Figure 1Z).

Expressions of key metabolic regulators, PGC1α and CPT1A in different precursor lesions of PDAC progression

Since our meta-analysis showed differential expression of PGC1α and CPT1A in PanINs and IPMNs, we performed tissue microarray (TMA) analysis of these markers using immunohistochemistry (IHC). The TMAs contain tissue samples of NP (n=6), chronic pancreatitis (CP) (n=15), PanIN1 (n=8), PanIN2 (n=3), PanIN3 (n=6), PanIN-derived PDAC (PanIN-PDAC or PDAC) (n=34), and pancreatic cystic neoplasms (PCNs), including IPMN (n=27), PDAC arising in IPMN (IPMN-PDAC) (n=27), serous cystic neoplasm (SC) (n=31), and mucinous cystic neoplasms (MCN) (n=21). The immunostaining showed that the NP expresses higher cytoplasmic and nuclear levels of PGC1α (Figure 2A). However, a significant decrease ($p<0.001$) in PGC1α expression was identified in PanIN1 samples ($p<0.001$; Figure 2A and B) compared to NP. However, PGC1α expression was gradually recovered in PanIN2 and PanIN3, followed by a complete re-appearance in PDAC (Figure 2A and B). Although we observed a reduced PGC1α expression in PanIN1 samples compared to NP, PanIN1 cells still retained low PGC1α expression (Figure 2A). By contrast, we found a significant increase ($p<0.02$) in cytoplasmic and nuclear PGC1α staining in IPMN and IPMN-PDAC compared to NP (Figure 2A). In addition, PGC1α expression localized differently in PanIN and IPMN. PGC1α expression was higher in the cytoplasm and lower in the nucleus of PanIN2; however, its expression was higher in both the cytoplasm and nucleus in IPMN (Figure 2C). On the other hand, SCs and MCNs maintained the same levels of PGC1α expression as observed in NP (Figure 2A and B).

Owing to the association of PGC1α with CPT1A (16–24), we sought to analyze CPT1A expression in PDAC progression samples. Compared with NP, CPT1A IHC staining was lower in PanIN1 and not significantly elevated in PanINs; however, its staining was significantly increased ($p<0.0001$) in IPMNs (Figure 2D and E). Interestingly, both PanIN-PDAC and IPMN-PDAC expressed significantly higher ($p<0.0001$) levels of CPT1A

(Figure 2D and E). The other PCNs, SC, and MCN, showed increased staining for CPT1A compared with NP ($p<0.0001$) (Figure 2D and E). PanIN and IPMN demonstrated differential subcellular localization of CPT1A expression. Faint CPT1A expression (not significant compared to NP) was localized to the cytoplasm in PanIN2, while IPMN demonstrated higher expression, localized to both the cytoplasm and nucleus (Figure 2F). These observations suggest that the expression of the FAO signature gene, CPT1A, is augmented in IPMN.

Stem cell signatures of ADM/PanINs and IPMN precursor lesions

To identify the stemness signature elevated during ADM/PanIN development, we induced ADM in wild-type (WT) and $KRAS^{G12D}$; Pdx-1 Cre (KC) mice by treating them with eight hourly intraperitoneal cerulean injections (75 μg/kg body weight) on two alternate days (Figure 3A). The mice were sacrificed two days after the last day of injection, and primary pancreatic cells were isolated. Isolated cells (Supplementary Figure 2A and B) were stained with FITC-conjugated Ulex Europaeus Agglutinin I (UEA1) (an acinar specific marker) and CD133 antibody, followed by sorting of acinar cells (UEA1+CD133-), acino-ductal (AD) cells (UEA1+CD133+), and ductal cells (UEA1-CD133+) (Figure 3B). The percentage of AD cells was significantly higher with cerulean treatment than in controls (Figure 3B and C). As expected, AD cells showed the loss of acinar cell markers, Amy1 and Cpa1, but gained the Krt19+ and Sox9+ phenotype (Figure 3D). The presence of Ptf1a, a promoter of acinar fate in AD cells even after the loss of Amy1 and Cpa1, confirms the intermediate de-differentiated state of the AD cells (Figure 3D). mRNA expression levels of stemness markers, Aldh1a1, Prom1 (Cd133), Paf1, and Epcam, were higher in sorted AD cells than acinar cells (Figure 3E and F). Besides, cerulean-induced AD cells showed a significantly increased sphere formation ability, suggesting that the AD cells display stemness characteristics (Figure 3G and H). Further, the induction of ADM in the pancreas of cerulean-treated WT mice was confirmed by immunofluorescence using ductal-specific FITC-conjugated lectin, Dolichos biflorus agglutinin (DBA), rhodamine-conjugated acinar-specific lectin, peanut agglutinin (PNA), FITC-conjugated acinar-specific lectin, UEA1, and antibodies for CD133 and PAF1 stemness markers (5). The pancreas tissue of cerulean-treated WT mice showed a loss of PNA or UEA1 staining and increased DBA or CD133 staining compared with pancreas from untreated mice, suggesting cerulean treatment-induced ADM (Figure 3I and Supplementary Figure 3A). We also found a reduced PAF1 expression in the cerulean-treated pancreas compared to control; however, the AD (PNA+DBA+ or CD133+UEA1+) cells still retained nuclear and cytoplasmic PAF1 expression, indicating stemness features (14) (Figure 3I and Supplementary Figure 3A–B). AldeRed assay also showed that the cerulean-induced AD cells had increased ALDH activity versus that in acinar cells from the untreated pancreas (Supplementary Figure 3C). Interestingly, the AD cells sorted from cerulean-treated KC mice (6 weeks old) (Supplementary Figure 4) showed elevated expression of Kit and decreased expression of Ctnnb1 compared with untreated KC pancreas (Figure 3J). Immunofluorescence staining also showed increased staining for cKIT and decreased staining of non-phospho active β-catenin (Figure 3K) in pancreas tissues harvested from 6-week-old cerulean-treated KC mice compared with untreated KC mice. Flow cytometry analysis showed an augmented percentage of cKIT+ cells in AD cells compared to acinar cells of KC mice (7 weeks

old) (Supplementary Figure 5). PanIN lesions of 10-week-old KC mice also showed a co-overexpression of cKIT and CD133 and decreased staining for non-phospho active β-catenin compared to the normal pancreas (Figure 3L).

To investigate the stemness signatures of IPMN, we used IPMN cell lines T161 and LGKC1 derived from the pancreas of KC^{Smad4-} and doxycycline-inducible Kras; Gnas (KG) mouse models, respectively. T161 cells showed a loss of Smad4 and increased ALDH1A1 protein expression levels compared to control KC cells (KC6141) (Figure 3M). AldeRed analysis also showed a higher percentage of ALDH+ cells in T161 cells than in KC6141 cells (Figure 3N–O). Immunofluorescence staining also showed increased expression of ALDH1A1 and CD133 stemness markers and decreased Smad4 in the IPMN regions of KC^{Smad4-} pancreas tissues compared to KC control (Figure 3P and Supplementary Figure 6). mRNA expression of Aldh1a1 and Sox2 stemness markers was higher in T161 cells than in KC6141 (Figure 3Q). Similarly, induction of Gnas in the LGKC1 cell line with doxycycline resulted in a marked upregulation of stemness genes such as Prom1, Sox2, Pou5f1, Nanog, Dclk1, and Ctnnb1 compared with untreated cells (Figure 3R and S). However, the induction of Gnas in LGKC1 cells did not elevate Kit expression (Figure 3S). Gnas induction also significantly increased the sphere formation ability of LGKC1 cells (Figure 3T and Supplementary Figure 7). Overall, these results suggest that stemness signatures are elevated in ADM/PanIN and IPMN.

Identification of FAO-dependent and FAO-independent OXPhos in IPMNs and ADM/PanINs, respectively

The meta-analysis and IHC analysis in previous sections suggest PGC1α and CPT1A are differentially expressed in IPMN and PanINs (Figure 1 and 2). Consistent with this data, cerulean-induced pancreas tissues of KC mice showed a significant reduction in PGC1α expression compared to the pancreas tissue of vehicle-treated mice by IHC (Figure 4A and B). Similarly, PGC1α and Cpt1a transcripts were decreased in the whole pancreas of cerulean-treated KC mice compared to control (Figure 4C–D and Supplementary Figure 8). Pancreatic cells isolated from cerulean-treated mice showed reductions in maximal respiration, spare respiratory capacity, glycolysis, glycolytic capacity, and FAO-mediated OXPhos (FAO-OXPhos) as analyzed by seahorse extracellular flux analyzer (Figure 4E–I).

Interestingly, PGC1α expression in KC mouse pancreas was reduced with cerulean treatment at the whole pancreas level (compared to control), while a small proportion of UEA1+ CD133+ AD cells still retained its expression (Figure 4J). However, cerulean-treated AD (PNA+DBA+) cells did not show CPT1A expression (Figure 4K). In addition, cerulean-induced and FACS-sorted AD cells showed increased mRNA levels of PGC1α and OXPhos genes (DLAT and ACO1) but reduced levels of Cpt1a compared with acinar cells (Figure 4L and M). Analysis of oxygen consumption rate (OCR) using Seahorse extracellular flux analyzer showed that basal OCR was elevated in AD cells (Figure 4N). PGC1α was co-overexpressed with cKIT and CD133 in PanIN lesions of the 10-week-old KC mouse pancreas compared to age-matched WT control (Figure 4O). The pancreas of 10-week-old KC mice also showed elevated DLAT expression with no CPT1A staining (Supplementary

Figure 9). These data suggest that the PanIN lesions and cerulean-induced AD cells express PGC1α and utilize FAO-independent OXPhos.

In contrast, Gnas induction in LGKC1 with doxycycline treatment (10 ng/ml) increased the mRNA levels of Ppargc1a, Cs, and FAO genes (Cpt1a, Cpt1b, Cpt1c, Acads) but decreased levels of Pdk1 compared with untreated LGKC1 (Figure 4P). Seahorse analysis showed that doxycycline treatment also elevated OCR levels in LGKC1 cells (Figure 4Q) but not in KC control cells (KC6141) (Supplementary Figure 10). Also, palmitate increased OCR only in doxycycline-induced LGKC1 cells but not in control LGKC1 cells (Figure 4Q). However, Gnas induction did not affect ECAR values compared to LGKC1 control cells (Figure 4R). Furthermore, human IPMN organoids showed co-expression of CPT1A and PGC1α (Figure 4S). Overall, these results indicate that IPMNs have FAO-dependent OXPhos and PGC1α expression.

ADM/PanINs and IPMN lesions upregulate unique PGC1α-interacting partners.

The ‘STRING’ software analysis of PGC1α protein-protein interactions showed the possible interaction of PGC1α with other co-receptors, including NRF1, PPARA, PPARG, NR1H3, ESRRA, RXRA, SIRT1, and CPT1A (Figure 5A). Gene expression analysis of the IPMN progression dataset (GSE19650) showed significant upregulation of PPARG and NRF1 in IPMNs (Figure 5B and C). Other PGC1α-interacting partners did not show upregulation in IPMN samples compared with the normal pancreas (Figure 5D–I). The AD cells sorted from the pancreas cells of the cerulean-treated KC mice (6 weeks old) showed increased Nrf1 and decreased Pprag expression compared with acinar cells (Figure 5J). Co-expression of PGC1α with PPARγ was observed in human IPMN organoids (Figure 5K). PGC1α was upregulated and coexpressed with nuclear PPARγ in doxycycline-induced LGKC1 cells and with nuclear as well as cytoplasmic NRF1 in cerulean-induced AD cells of KC mice (Figure 5L–N). PanIN lesions of 10-week-old KC mice also showed co-expression of PGC1α with NRF1 (Figure 5O). These data collectively suggest that ADM/PanINs and IPMNs overexpress PGC1α-interacting partners, NRF1 and PPARγ, respectively.

PGC1α controls stemness through FAO-dependent and FAO-independent OXPhos in IPMN and ADM/PanINs, respectively

We first sought to examine the role of PGC1α in pancreatic tumorigenesis. For this, we generated Colo357 PDAC cells and LGKC1 cells (Figure 6A and Supplementary Figure 11A) with stable PGC1α knockdown (KD) using a PGC1α shRNA followed by subcutaneous implantation in nude mice. A significant decrease in tumor weight and tumor volume was observed in the PGC1α KD groups compared to scramble control (Supplementary Figure 11B–D and Figure 6B). KD of PGC1α reduced the expression of the ALDH1A1 stemness marker in Colo357 cells (Supplementary Figure 11A). Similarly, PGC1α KD in LGKC1 cells reduced Gnas-induced overexpression of stemness genes (Prom1 and Ctnnb1) and FAO gene, Cpt1a (Figure 6C). We also inhibited PGC1α expression in LGKC1 cells using its selective inhibitor, SR18292. SR18292 increases the interaction between GCN5, an acetyltransferase, and PGC1α, increasing its acetylation and inhibition (25). SR18292 has been shown to diminish tumor growth by inhibiting PGC1α-mediated OXPhos in multiple myeloma (26), and ameliorate diabetes (27) without

signs of toxicity. Treatment of LGKC1 cells with SR18292 increased the levels of acetylated PGC1α (Supplementary Figure 12). Our data showed that SR18292 corrected the OCR levels increased by the addition of palmitate in Gnas-induced LGKC1 cells, indicating that PGC1α contributes to the elevation of Gnas-induced FAO-OXPhos (Figure 6D–F). However, SR18292 did not affect glycolysis and glycolytic capacity (Supplementary Figure 13A and B). Interestingly, SR18292 significantly reduced the effects of Gnas on Prom1 expression (Supplementary Figure 14), sphere formation ability (Supplementary Figure 15A and B), and size of human IPMN organoids (Figure 6G–H and Supplementary Figure 16). Further, SR18292 decreased Gnas-induced PGC1α and PPARγ levels (Supplementary Figure 17). Immunofluorescence staining on human IPMN organoids showed that treatment with SR18292 reduced the expression of PGC1α, CPT1A, and PPARγ (Figure 6I and J). On the other hand, SR18292 significantly reduced the number of duct-like structures in 3D Matrigel cultures of primary pancreatic acinar cells isolated from 9-week-old KC mice (Figure 6K). It also reduced gene expression of ductal marker (Krt19), stemness markers (Kit and Prom1), and OXPhos marker (Dlat) (Figure 6L). Similarly, SR18292 treatment significantly inhibited the sphere-forming capacity of cerulean-induced AD cells (Figure 6M), along with staining for Mitotracker Deep Red FM (a dye that stains mitochondrial mass) (Figure 6N). To conclude, PGC1α controls stemness signatures through FAO-dependent and FAO-independent OXPhos in IPMNs and ADMPanINs, respectively (Figure 7).

Discussion

PDAC is one of the most lethal diseases, and its high mortality rate is due to a lack of specific early diagnostic tools. Two major PPLs, ADM-PanIN and IPMN, are responsible for PDAC development; however, the early detection of these PPLs is still challenging as knowledge about the molecular signatures of these PPLs is inadequate (1). Extensive metabolic reprogramming and emergence of cancer stem cells (CSCs) are two of several factors contributing to the aggressiveness of advanced PDAC. We and others have previously shown that the CSCs in advanced tumors exhibit specific metabolic signatures, and the inhibition of a particular metabolic program diminishes CSC survival (11,12). We observed aerobic glycolysis, OXPhos, and FAO-OXPhos as the major metabolic signatures of pancreatic CSC populations (11). However, the stemness and metabolic signatures of pancreatic precursor lesions (PPLs) and how they regulate the initiation events of PDAC are unknown. Here, we demonstrated that the ADM/PanINs and IPMNs show FAO-independent OXPhos and FAO-dependent OXPhos (FAO-OXPhos), respectively, correlating with specific stemness signatures. We showed that PGC1α-mediated OXPhos and FAO-OXPhos govern the specific stemness phenotype of PPLs. Also, PGC1α knockdown using shRNA or inhibition using SR18292 reduced *in vivo* tumorigenicity and repressed stemness features by targeting OXPhos and FAO-OXPhos in ADM/PanINs and IPMN, respectively.

Several lines of evidence suggest that CSCs play a critical role in the initiation and progression of PDAC (28,29). CSCs share similar characteristics as normal stem or progenitor cells, such as self-renewal and multi-lineage differentiation. Recent lineage-tracing studies demonstrated that stem/progenitor cells with mutation(s) contribute to the initiation and development of cancers. For instance, APC-mutant Lgr5+ stem cells have

been involved in the initiation and development of intestinal adenomas (6,9). Aldh1b1- and Nestin-positive pancreatic stem/progenitor cells are highly responsive to Kras oncogenic activation and Kras-mediated tumorigenesis (7,8). Despite these studies, the exact stemness signatures of ADM/PanINs and IPMN and how the stemness is regulated in PPLs are unknown. Our data showed that ADM/PanINs and IPMNs express overlapping sets of stemness genes. Both the PanINs and IPMNs overexpressed PROM1, ALDH2, LIF, NANOG, and KLF4. In addition, the ADM/PanINs showed a KIT, NOTCH2, and CD34 stemness signature, which did not include CTNNB1. In agreement with this observation, previous studies suggested that the loss of β-catenin is required for Kras-induced ADM and PanIN development (30,31). In contrast, IPMNs showed an exclusive expression of CTNNB1 and ALDH3A1 stemness genes, in concordance with a previous study (32). Overall, ADM/PanINs and IPMN express specific stemness signatures.

Metabolic reprogramming is a significant event that occurs during cellular transformation (33). CSCs in advanced tumors are regulated by a specific metabolic program (12,34–42). Our previous study identified significant upregulation of metabolic modulator PGC1α in pancreatic CSCs (11). Also, silencing of PGC1α in pancreatic CSCs reduced mitochondrial activity and CSC self-renewal, suggesting a critical role of PGC1α in pancreatic CSCs (12). The role of PGC1α in diabetes, obesity, and cardiovascular disease (CVD) is well established (43); however, its importance in cancer has not been thoroughly explored. In breast cancer, increased PGC1α expression is associated with elevated metastasis and poor prognosis (44,45). However, elevated PGC1α levels in prostate cancer are associated with low metastasis and a good prognosis (46). In melanoma, a PGC1α-high subpopulation showed increased OXPhos, reduced glycolysis, and low invasion, while PGC1α-low melanoma cells displayed decreased OXPhos, increased glycolysis, and elevated invasion (47,48). However, the role of PGC1α in PDAC development and progression is unknown.

Our meta-analysis and TMA data followed by *in vitro and in vivo* validation studies suggested that the expression of PGC1α was significantly elevated in IPMN. In contrast, its expression was reduced in clinical samples of early PanINs (PanIN1) compared to the normal pancreas. However, PGC1α expression re-appeared in PanIN3 and PanIN-derived PDAC. Interestingly, PanIN1 cells still maintained low PGC1α expression. These observations were recapitulated during cerulean-induced ADM and spontaneous PanIN development in the pancreas of mice with activated $Kras^{G12D}$ background. The PanINs and cerulean-induced ADM in mice with mutant Kras showed a reduced PGC1α expression compared to wild-type controls; however, a few AD metaplastic cells and PanINs still retained low PGC1α expression. A large body of evidence suggests that PanINs emerge during human and mouse PDAC development (49–52). In mouse models of PDAC development, acinar-to-ductal metaplastic changes or ADM is often observed as a pre-precursor lesion of PanIN development (51,53–57). A previous non-genetic *in vitro* lineage tracing study showed that human acinar cells could also differentiate into duct-like cells (54). Another study suggested that TGFβ could induce ADM in human pancreatic acinar cells *in vitro* (58). Despite these two pieces of evidence, the ADM process in human PDAC development is not well defined. The propensity of these AD metaplastic cells and PanIN cells (both expressing low PGC1α) to form advanced PanINs and subsequently progress to PDAC needs to be further explored in future studies.

Recent studies have demonstrated a clear correlation between the PGC1α/CPT1A axis and FAO-mediated OXPhos in diabetes, obesity, and cancer (16–24). Owing to the association of PGC1α with CPT1A, we analyzed CPT1A expression in PDAC progression samples. Interestingly, our meta- and IHC analyses revealed that CPT1A expression levels are elevated in IPMN but not in PanIN samples, suggesting the reliance of IPMNs on FAO-OXPhos. Interestingly, advanced PDAC samples of PanIN or IPMN origin showed increased levels of CPT1A expression, potentially due to the metabolic heterogeneity of these advanced tumors.

Further validation of these meta-analyses and IHC data using *in vitro* and *in vivo* models showed increased OXPhos and reduced CPT1A expression or FAO-OXPhos in AD metaplastic cells. The AD cells also showed elevated expression of DLAT, a gene that encodes the E2 component of the pyruvate dehydrogenase complex (PDC). The PDC catalyzes pyruvate conversion to acetyl coenzyme A, which enters the Krebs cycle. Further, PanIN lesions of 10-week-old KC mice showed elevated DLAT expression with low CPT1A expression. In contrast, IPMN showed elevated FAO-OXPhos and increased expression of FAO genes, CPT1A, CPT1B, CPT1C, and ACADS. These observations indicate that ADM/PanINs and IPMNs utilize FAO-independent and FAO-dependent OXPhos, respectively.

To examine whether PGC1α regulates the stemness programs and metabolic signatures of ADM/PanINs and IPMN, we knocked down PGC1α or inhibited its activity using SR18292. PGC1α KD significantly reduced *in vivo* tumorigenicity of PDAC and IPMN cells, suggesting a tumorigenic role of PGC1α. PGC1α KD also reduced the Gnas-induced stemness signature (CTNNB1 and CD133) and metabolic signature (CPT1A) of IPMN. Previous studies demonstrated that SR18292 disrupts OXPhos by acetylating PGC1α in multiple myeloma cells and chronic myeloid leukemia (CML) stem cells, leading to the inhibition of tumor growth (26,59). Consistent with these studies, our findings showed that SR18292 acetylated PGC1α and inhibited FAO-OXPhos in IPMN. SR18292 also inhibited stemness signatures, including the expression of CD133 and self-renewal in IPMN, and reduced human IPMN organoid size. These data suggest that PGC1α-mediated FAO-OXPhos governs the specific stemness program in IPMN.

Since the mice with mutant Kras background begin to develop early PanINs spontaneously by 8–10 weeks of age (52,60), we isolated primary pancreatic cells from 9-week-old KC mice, cultured them in 3D Matrigel, and treated them with SR18292. SR18292 reduced the number of duct-like structures and diminished the expression levels of ductal (Krt19), stemness (Kit and Prom1), and OXPhos (Dlat) genes. SR18292 also inhibited the mitochondrial mass and self-renewal of cerulean-induced AD cells. These data suggest that the PGC1α-mediated OXPhos regulates the stemness features of ADM/PanINs.

Our next goal was to delineate how PGC1α regulates two distinct metabolic pathways (FAO-independent and FAO-dependent) of ADM/PanINs and IPMN. PGC1α requires its coactivator proteins to regulate mitochondrial biogenesis, OXPhos, FAO-OXPhos, and CPT1A expression (17–24). In nasopharyngeal carcinoma, PGC1α has been shown to interact with CEBPB, inducing CPT1A expression and radiation resistance (61). Studies also showed that PGC1α interacts with NRF1 and regulates mitochondrial biogenesis

and OXPhos. Through its interaction with PPARγ, PGC1α regulates FAO-OXPhos, and CPT1A expression (62,63). Our meta-analysis of human IPMN samples and gene expression analysis of mouse AD metaplastic cells showed an upregulation of PPARγ and NRF1 in IPMN and ADM, respectively, accompanied by co-overexpression of PGC1α. Interestingly, the inhibition of PGC1α with SR18292 reduced the expression of PPARγ in IPMN, suggesting a strong association of PGC1α with PPARγ. Thus, our observations and previous studies indicate that PGC1α differentially regulates the unique metabolic programs of ADM/PanIN and IPMN by interacting with NRF1 and PPARγ, respectively: a concept that needs to be further explored.

In conclusion, this study identified specific metabolic signatures of two major PPLs, ADM/PanIN and IPMN, in PDAC development. We suggest for the first time that the central modulator of energy metabolism, PGC1α, regulates the specific stemness of the PPLs by upregulating specific metabolic programs. This study also showed for the first time in solid cancers that a selective PGC1α inhibitor, SR18292, can repress stemness by targeting OXPhos/FAO-OXPhos in these early events of PDAC progression. This study serves as a stepping stone for future research developing novel early PDAC detection tools and anti-CSC therapeutic strategies.

Supplementary Material

Refer to Web version on PubMed Central for supplementary material.

Acknowledgments

We thank Corinn E. Grabow for all the technical support. We thank Craig Semerad, Victoria B. Smith, and Samantha Wall of the Flow Cytometry Research Facility, University of Nebraska Medical Center, for assisting with flow cytometry. We thank Dr. Anirban Maitra, MD Anderson Cancer Center, for providing the LGKC1 cell line. (This work was supported, in part, by the National Institutes of Health (P01 CA217798, R01 CA183459, R01 CA195586, R01 CA210637, U01 CA200466, and U01 CA210240). We thank Jessica Mercer for the editorial contribution to the manuscript.

References

1. Distler M, Aust D, Weitz J, Pilarsky C, Grützmann R. Precursor lesions for sporadic pancreatic cancer: PanIN, IPMN, and MCN. Biomed Res Int 2014;2014:474905– doi 10.1155/2014/474905. [PubMed: 24783207]
2. Bardeesy N, Aguirre AJ, Chu GC, Cheng K-h, Lopez LV, Hezel AF, et al. Both p16(Ink4a) and the p19(Arf)-p53 pathway constrain progression of pancreatic adenocarcinoma in the mouse. Proc Natl Acad Sci U S A 2006;103(15):5947–52 doi 10.1073/pnas.0601273103. [PubMed: 16585505]
3. Ideno N, Yamaguchi H, Ghosh B, Gupta S, Okumura T, Steffen DJ, et al. GNAS(R201C) Induces Pancreatic Cystic Neoplasms in Mice That Express Activated KRAS by Inhibiting YAP1 Signaling. Gastroenterology 2018;155(5):1593–607.e12 doi 10.1053/j.gastro.2018.08.006. [PubMed: 30142336]
4. Omori Y, Ono Y, Tanino M, Karasaki H, Yamaguchi H, Furukawa T, et al. Pathways of Progression From Intraductal Papillary Mucinous Neoplasm to Pancreatic Ductal Adenocarcinoma Based on Molecular Features. Gastroenterology 2019;156(3):647–61.e2 doi 10.1053/j.gastro.2018.10.029. [PubMed: 30342036]
5. Nimmakayala RK, Seshacharyulu P, Lakshmanan I, Rachagani S, Chugh S, Karmakar S, et al. Cigarette Smoke Induces Stem Cell Features of Pancreatic Cancer Cells via PAF1. Gastroenterology 2018;155(3):892–908.e6 doi 10.1053/j.gastro.2018.05.041. [PubMed: 29864419]

6. Buczacki SJA, Zecchini HI, Nicholson AM, Russell R, Vermeulen L, Kemp R, et al. Intestinal label-retaining cells are secretory precursors expressing Lgr5. Nature 2013;495(7439):65–9 doi 10.1038/nature11965. [PubMed: 23446353]
7. Carrière C, Seeley ES, Goetze T, Longnecker DS, Korc M. The Nestin progenitor lineage is the compartment of origin for pancreatic intraepithelial neoplasia. Proceedings of the National Academy of Sciences of the United States of America 2007;104(11):4437–42 doi 10.1073/pnas.0701117104. [PubMed: 17360542]
8. Mameishvili E, Serafimidis I, Iwaszkiewicz S, Lesche M, Reinhardt S, Bölicke N, et al. Aldh1b1 expression defines progenitor cells in the adult pancreas and is required for Kras-induced pancreatic cancer. Proceedings of the National Academy of Sciences of the United States of America 2019;116(41):20679–88 doi 10.1073/pnas.1901075116. [PubMed: 31548432]
9. Schepers AG, Snippert HJ, Stange DE, van den Born M, van Es JH, van de Wetering M, et al. Lineage tracing reveals Lgr5+ stem cell activity in mouse intestinal adenomas. Science (New York, NY) 2012;337(6095):730–5 doi 10.1126/science.1224676.
10. Biancur DE, Kimmelman AC. The plasticity of pancreatic cancer metabolism in tumor progression and therapeutic resistance. Biochim Biophys Acta Rev Cancer 2018;1870(1):67–75 doi 10.1016/j.bbcan.2018.04.011. [PubMed: 29702208]
11. Nimmakayala RK, Leon F, Rachagani S, Rauth S, Nallasamy P, Marimuthu S, et al. Metabolic programming of distinct cancer stem cells promotes metastasis of pancreatic ductal adenocarcinoma. Oncogene 2020 doi 10.1038/s41388-020-01518-2.
12. Sancho P, Burgos-Ramos E, Tavera A, Bou Kheir T, Jagust P, Schoenhals M, et al. MYC/PGC-1alpha Balance Determines the Metabolic Phenotype and Plasticity of Pancreatic Cancer Stem Cells. Cell Metab 2015;22(4):590–605 doi 10.1016/j.cmet.2015.08.015. [PubMed: 26365176]
13. Kaushik G, Seshacharyulu P, Rauth S, Nallasamy P, Rachagani S, Nimmakayala RK, et al. Selective inhibition of stemness through EGFR/FOXA2/SOX9 axis reduces pancreatic cancer metastasis. Oncogene 2020 doi 10.1038/s41388-020-01564-w.
14. Dey P, Rachagani S, Vaz AP, Ponnusamy MP, Batra SK. PD2/Paf1 depletion in pancreatic acinar cells promotes acinar-to-ductal metaplasia. Oncotarget 2014;5(12):4480–91 doi 10.18632/oncotarget.2041. [PubMed: 24947474]
15. Öhlund D, Handly-Santana A, Biffi G, Elyada E, Almeida AS, Ponz-Sarvise M, et al. Distinct populations of inflammatory fibroblasts and myofibroblasts in pancreatic cancer. J Exp Med 2017;214(3):579–96 doi 10.1084/jem.20162024. [PubMed: 28232471]
16. Du Q, Tan Z, Shi F, Tang M, Xie L, Zhao L, et al. PGC1α/CEBPB/CPT1A axis promotes radiation resistance of nasopharyngeal carcinoma through activating fatty acid oxidation. Cancer Sci 2019;110(6):2050–62 doi 10.1111/cas.14011. [PubMed: 30945396]
17. Mootha VK, Lindgren CM, Eriksson KF, Subramanian A, Sihag S, Lehar J, et al. PGC-1alpha-responsive genes involved in oxidative phosphorylation are coordinately downregulated in human diabetes. Nat Genet 2003;34(3):267–73 doi 10.1038/ng1180. [PubMed: 12808457]
18. Zhang Y, Ma K, Song S, Elam MB, Cook GA, Park EA. Peroxisomal proliferator-activated receptor-gamma coactivator-1 alpha (PGC-1 alpha) enhances the thyroid hormone induction of carnitine palmitoyltransferase I (CPT-I alpha). J Biol Chem 2004;279(52):53963–71 doi 10.1074/jbc.M406028200. [PubMed: 15469941]
19. Wu Y, Delerive P, Chin WW, Burris TP. Requirement of helix 1 and the AF-2 domain of the thyroid hormone receptor for coactivation by PGC-1. J Biol Chem 2002;277(11):8898–905 doi 10.1074/jbc.M110761200. [PubMed: 11751919]
20. Schreiber SN, Emter R, Hock MB, Knutti D, Cardenas J, Podvinec M, et al. The estrogen-related receptor alpha (ERRalpha) functions in PPARgamma coactivator 1alpha (PGC-1alpha)-induced mitochondrial biogenesis. Proceedings of the National Academy of Sciences of the United States of America 2004;101(17):6472–7 doi 10.1073/pnas.0308686101. [PubMed: 15087503]
21. Mootha VK, Handschin C, Arlow D, Xie X, St Pierre J, Sihag S, et al. Erralpha and Gabpa/b specify PGC-1alpha-dependent oxidative phosphorylation gene expression that is altered in diabetic muscle. Proceedings of the National Academy of Sciences of the United States of America 2004;101(17):6570–5 doi 10.1073/pnas.0401401101. [PubMed: 15100410]

22. Wang YX, Lee CH, Tiep S, Yu RT, Ham J, Kang H, et al. Peroxisome-proliferator-activated receptor delta activates fat metabolism to prevent obesity. Cell 2003;113(2):159–70 doi 10.1016/s0092-8674(03)00269-1. [PubMed: 12705865]
23. Vega RB, Huss JM, Kelly DP. The coactivator PGC-1 cooperates with peroxisome proliferator-activated receptor alpha in transcriptional control of nuclear genes encoding mitochondrial fatty acid oxidation enzymes. Mol Cell Biol 2000;20(5):1868–76 doi 10.1128/mcb.20.5.1868-1876.2000. [PubMed: 10669761]
24. Wu Z, Puigserver P, Andersson U, Zhang C, Adelmant G, Mootha V, et al. Mechanisms controlling mitochondrial biogenesis and respiration through the thermogenic coactivator PGC-1. Cell 1999;98(1):115–24 doi 10.1016/s0092-8674(00)80611-x. [PubMed: 10412986]
25. Sharabi K, Lin H, Tavares CDJ, Dominy JE, Camporez JP, Perry RJ, et al. Selective Chemical Inhibition of PGC-1α Gluconeogenic Activity Ameliorates Type 2 Diabetes. Cell 2017;169(1):148–60.e15 doi 10.1016/j.cell.2017.03.001. [PubMed: 28340340]
26. Xiang Y, Fang B, Liu Y, Yan S, Cao D, Mei H, et al. SR18292 exerts potent antitumor effects in multiple myeloma via inhibition of oxidative phosphorylation. Life Sci 2020;256:117971 doi 10.1016/j.lfs.2020.117971. [PubMed: 32553925]
27. Crunkhorn S Identification of novel Aβ inhibitors. Nature Reviews Drug Discovery 2017;16(2):88– doi 10.1038/nrd.2017.10. [PubMed: 28148931]
28. Hermann PC, Huber SL, Herrler T, Aicher A, Ellwart JW, Guba M, et al. Distinct populations of cancer stem cells determine tumor growth and metastatic activity in human pancreatic cancer. Cell Stem Cell 2007;1(3):313–23 doi 10.1016/j.stem.2007.06.002. [PubMed: 18371365]
29. Niess H, Camaj P, Renner A, Ischenko I, Zhao Y, Krebs S, et al. Side population cells of pancreatic cancer show characteristics of cancer stem cells responsible for resistance and metastasis. Target Oncol 2015;10(2):215–27 doi 10.1007/s11523-014-0323-z. [PubMed: 24950733]
30. Criscimanna A, Duan LJ, Rhodes JA, Fendrich V, Wickline E, Hartman DJ, et al. PanIN-specific regulation of Wnt signaling by HIF2α during early pancreatic tumorigenesis. Cancer research 2013;73(15):4781–90 doi 10.1158/0008-5472.Can-13-0566. [PubMed: 23749643]
31. Morris JPt Cano DA, Sekine S Wang SC, Hebrok M. Beta-catenin blocks Kras-dependent reprogramming of acini into pancreatic cancer precursor lesions in mice. The Journal of clinical investigation 2010;120(2):508–20 doi 10.1172/jci40045. [PubMed: 20071774]
32. Chetty R, Serra S, Salahshor S, Alsaad K, Shih W, Blaszyk H, et al. Expression of Wnt-signaling pathway proteins in intraductal papillary mucinous neoplasms of the pancreas: a tissue microarray analysis. Human pathology 2006;37(2):212–7 doi 10.1016/j.humpath.2005.11.002. [PubMed: 16426922]
33. Spyrou J, Gardner DK, Harvey AJ. Metabolism Is a Key Regulator of Induced Pluripotent Stem Cell Reprogramming. Stem cells international. Volume 20192019. p 7360121.
34. Ciavardelli D, Rossi C, Barcaroli D, Volpe S, Consalvo A, Zucchelli M, et al. Breast cancer stem cells rely on fermentative glycolysis and are sensitive to 2-deoxyglucose treatment. Cell Death Dis 2014;5:e1336 doi 10.1038/cddis.2014.285. [PubMed: 25032859]
35. De Luca A, Fiorillo M, Peiris-Pages M, Ozsvari B, Smith DL, Sanchez-Alvarez R, et al. Mitochondrial biogenesis is required for the anchorage-independent survival and propagation of stem-like cancer cells. Oncotarget 2015;6(17):14777–95 doi 10.18632/oncotarget.4401. [PubMed: 26087310]
36. Jagust P, de Luxán-Delgado B, Parejo-Alonso B, Sancho P. Metabolism-Based Therapeutic Strategies Targeting Cancer Stem Cells. Frontiers in pharmacology 2019;10:203– doi 10.3389/fphar.2019.00203. [PubMed: 30967773]
37. Lamb R, Bonuccelli G, Ozsvari B, Peiris-Pages M, Fiorillo M, Smith DL, et al. Mitochondrial mass, a new metabolic biomarker for stem-like cancer cells: Understanding WNT/FGF-driven anabolic signaling. Oncotarget 2015;6(31):30453–71 doi 10.18632/oncotarget.5852. [PubMed: 26421711]
38. Liao J, Qian F, Tchabo N, Mhawech-Fauceglia P, Beck A, Qian Z, et al. Ovarian cancer spheroid cells with stem cell-like properties contribute to tumor generation, metastasis and chemotherapy resistance through hypoxia-resistant metabolism. PLoS One 2014;9(1):e84941 doi 10.1371/journal.pone.0084941. [PubMed: 24409314]

39. Luo M, Shang L, Brooks MD, Jiagge E, Zhu Y, Buschhaus JM, et al. Targeting Breast Cancer Stem Cell State Equilibrium through Modulation of Redox Signaling. Cell Metab 2018;28(1):69–86.e6 doi 10.1016/j.cmet.2018.06.006. [PubMed: 29972798]
40. Luo M, Wicha MS. Targeting Cancer Stem Cell Redox Metabolism to Enhance Therapy Responses. Seminars in radiation oncology 2019;29(1):42–54 doi 10.1016/j.semradonc.2018.10.003. [PubMed: 30573183]
41. Pasto A, Bellio C, Pilotto G, Ciminale V, Silic-Benussi M, Guzzo G, et al. Cancer stem cells from epithelial ovarian cancer patients privilege oxidative phosphorylation, and resist glucose deprivation. Oncotarget 2014;5(12):4305–19 doi 10.18632/oncotarget.2010. [PubMed: 24946808]
42. Zhou Y, Zhou Y, Shingu T, Feng L, Chen Z, Ogasawara M, et al. Metabolic alterations in highly tumorigenic glioblastoma cells: preference for hypoxia and high dependency on glycolysis. J Biol Chem 2011;286(37):32843–53 doi 10.1074/jbc.M111.260935. [PubMed: 21795717]
43. Liang H, Ward WF. PGC-1alpha: a key regulator of energy metabolism. Advances in physiology education 2006;30(4):145–51 doi 10.1152/advan.00052.2006. [PubMed: 17108241]
44. LeBleu VS, O'Connell JT, Gonzalez Herrera KN, Wikman H, Pantel K, Haigis MC, et al. PGC-1α mediates mitochondrial biogenesis and oxidative phosphorylation in cancer cells to promote metastasis. Nature cell biology 2014;16(10):992–1003, 1–15 doi 10.1038/ncb3039. [PubMed: 25241037]
45. Andrzejewski S, Klimcakova E, Johnson RM, Tabariès S, Annis MG, McGuirk S, et al. PGC-1α Promotes Breast Cancer Metastasis and Confers Bioenergetic Flexibility against Metabolic Drugs. Cell metabolism 2017;26(5):778–87.e5 doi 10.1016/j.cmet.2017.09.006. [PubMed: 28988825]
46. Torrano V, Valcarcel-Jimenez L, Cortazar AR, Liu X, Urosevic J, Castillo-Martin M, et al. The metabolic co-regulator PGC1α suppresses prostate cancer metastasis. Nature cell biology 2016;18(6):645–56 doi 10.1038/ncb3357. [PubMed: 27214280]
47. Vazquez F, Lim JH, Chim H, Bhalla K, Girnun G, Pierce K, et al. PGC1α expression defines a subset of human melanoma tumors with increased mitochondrial capacity and resistance to oxidative stress. Cancer cell 2013;23(3):287–301 doi 10.1016/j.ccr.2012.11.020. [PubMed: 23416000]
48. Luo C, Lim JH, Lee Y, Granter SR, Thomas A, Vazquez F, et al. A PGC1α-mediated transcriptional axis suppresses melanoma metastasis. Nature 2016;537(7620):422–6 doi 10.1038/nature19347. [PubMed: 27580028]
49. Hruban RH, Maitra A, Kern SE, Goggins M. Precursors to Pancreatic Cancer. Gastroenterology Clinics of North America 2007;36(4):831–49. [PubMed: 17996793]
50. Cooper CL, O'Toole SA, Kench JG. Classification, morphology and molecular pathology of premalignant lesions of the pancreas. Pathology 2013;45(3):286–304. [PubMed: 23442735]
51. Shen R, Wang Q, Cheng S, Liu T, Jiang H, Zhu J, et al. The biological features of PanIN initiated from oncogenic Kras mutation in genetically engineered mouse models. Cancer letters 2013;339(1):135–43 doi 10.1016/j.canlet.2013.07.010. [PubMed: 23887057]
52. Westphalen CB, Olive KP. Genetically engineered mouse models of pancreatic cancer. Cancer journal (Sudbury, Mass) 2012;18(6):502–10 doi 10.1097/PPO.0b013e31827ab4c4.
53. Kopp JL, von Figura G, Mayes E, Liu FF, Dubois CL, Morris JPt, et al. Identification of Sox9-dependent acinar-to-ductal reprogramming as the principal mechanism for initiation of pancreatic ductal adenocarcinoma. Cancer cell 2012;22(6):737–50 doi 10.1016/j.ccr.2012.10.025. [PubMed: 23201164]
54. Houbracken I, de Waele E, Lardon J, Ling Z, Heimberg H, Rooman I, et al. Lineage tracing evidence for transdifferentiation of acinar to duct cells and plasticity of human pancreas. Gastroenterology 2011;141(2):731–41, 41.e1–4 doi 10.1053/j.gastro.2011.04.050. [PubMed: 21703267]
55. Shi G, Zhu L, Sun Y, Bettencourt R, Damsz B, Hruban RH, et al. Loss of the acinar-restricted transcription factor Mist1 accelerates Kras-induced pancreatic intraepithelial neoplasia. Gastroenterology 2009;136(4):1368–78 doi 10.1053/j.gastro.2008.12.066. [PubMed: 19249398]
56. Habbe N, Shi G, Meguid RA, Fendrich V, Esni F, Chen H, et al. Spontaneous induction of murine pancreatic intraepithelial neoplasia (mPanIN) by acinar cell targeting of oncogenic Kras

in adult mice. Proceedings of the National Academy of Sciences of the United States of America 2008;105(48):18913–8 doi 10.1073/pnas.0810097105. [PubMed: 19028870]

57. De La OJ, Emerson LL, Goodman JL, Froebe SC, Illum BE, Curtis AB, et al. Notch and Kras reprogram pancreatic acinar cells to ductal intraepithelial neoplasia. Proceedings of the National Academy of Sciences of the United States of America 2008;105(48):18907–12 doi 10.1073/pnas.0810111105. [PubMed: 19028876]
58. Liu J, Akanuma N, Liu C, Naji A, Halff GA, Washburn WK, et al. TGF-β1 promotes acinar to ductal metaplasia of human pancreatic acinar cells. Scientific reports 2016;6:30904 doi 10.1038/srep30904. [PubMed: 27485764]
59. Abraham A, Qiu S, Chacko BK, Li H, Paterson A, He J, et al. SIRT1 regulates metabolism and leukemogenic potential in CML stem cells. The Journal of clinical investigation 2019;129(7):2685–701 doi 10.1172/jci127080. [PubMed: 31180336]
60. Rachagani S, Torres MP, Kumar S, Haridas D, Baine M, Macha MA, et al. Mucin (Muc) expression during pancreatic cancer progression in spontaneous mouse model: potential implications for diagnosis and therapy. Journal of hematology & oncology 2012;5:68 doi 10.1186/1756-8722-5-68. [PubMed: 23102107]
61. Du Q, Tan Z, Shi F, Tang M, Xie L, Zhao L, et al. PGC1alpha/CEBPB/CPT1A axis promotes radiation resistance of nasopharyngeal carcinoma through activating fatty acid oxidation. Cancer Sci 2019;110(6):2050–62 doi 10.1111/cas.14011. [PubMed: 30945396]
62. Bost F, Kaminski L. The metabolic modulator PGC-1α in cancer. Am J Cancer Res 2019;9(2):198–211. [PubMed: 30906622]
63. Sharma S, Sun X, Rafikov R, Kumar S, Hou Y, Oishi PE, et al. PPAR-γ Regulates Carnitine Homeostasis and Mitochondrial Function in a Lamb Model of Increased Pulmonary Blood Flow. PLOS ONE 2012;7(9):e41555 doi 10.1371/journal.pone.0041555. [PubMed: 22962578]

Translational relevance

Pancreatic ductal adenocarcinoma (PDAC), recognized as a lethal disease, is developed mainly from two pancreatic precursor lesions (PPLs): acinar-to-ductal metaplasia (ADM)-mediated pancreatic intraepithelial neoplasms (PanINs) and intraductal papillary mucinous neoplasm (IPMN). Cancer stem cells (CSCs) drive PDAC tumors' aggressiveness, and unique metabolic programs regulate CSCs. However, regulation of the stemness and metabolic programs in PPLs is unknown. Our meta-analysis, *in vitro* results, and *in vivo* data demonstrate that the ADM/PanINs and IPMNs display fatty acid β-oxidation (FAO)-independent and FAO-dependent oxidative phosphorylation (OXPhos), respectively, and show specific stemness signatures. We identified the peroxisome proliferator-activated receptor γ isoform α (PGC1α) as a significant regulator of unique metabolism and stemness of ADM/PanINs and IPMN. The knockdown of PGC1α or its inhibition using SR18292 repressed the specific metabolism and stemness in PPLs. Thus, this study paves the way for developing a novel PDAC therapy based on targeting metabolism and stemness using PGC1α inhibitor, SR18292.

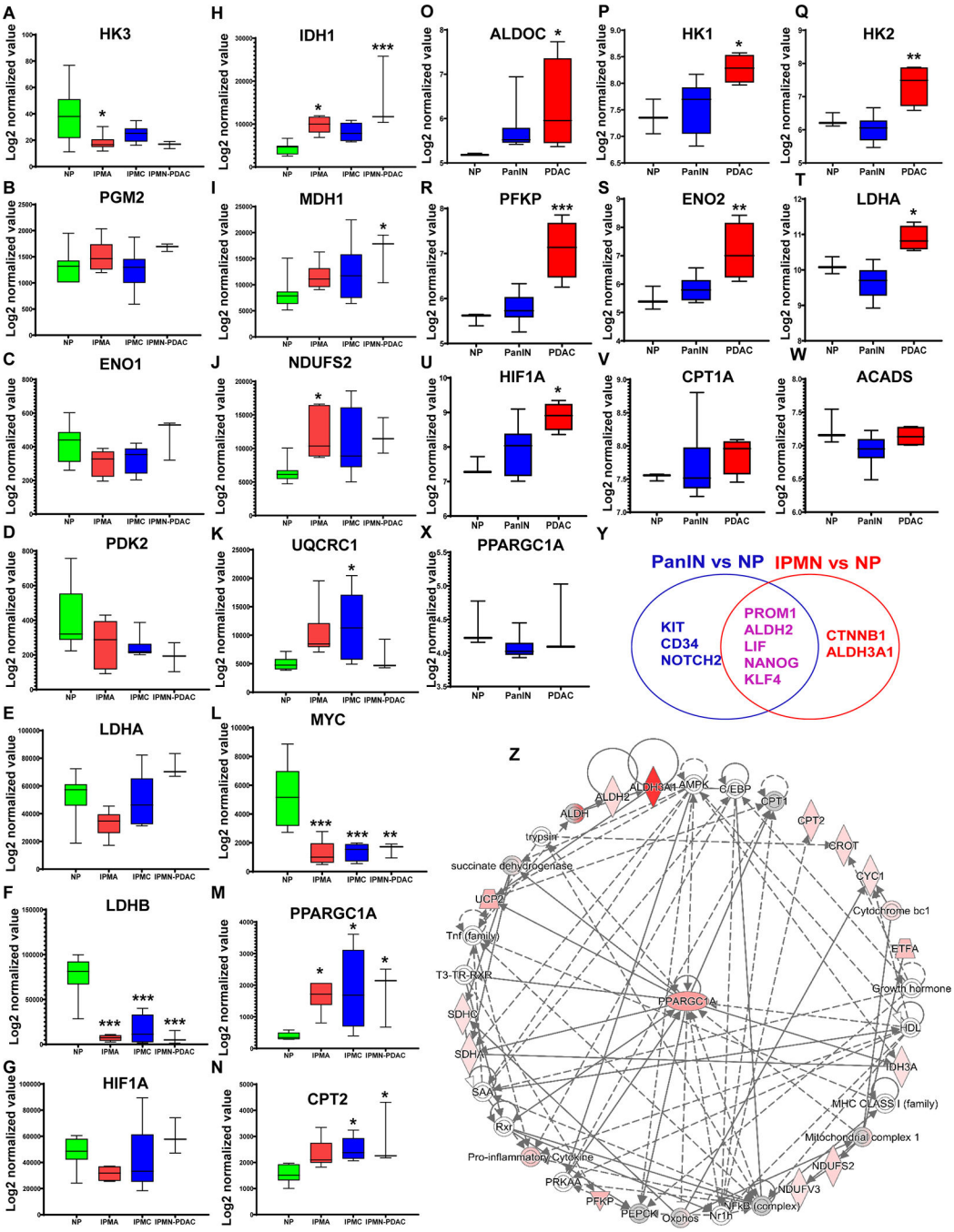

Figure 1. Meta-analysis of stemness programs and metabolic states in IPMN- and PanIN-mediated PDAC progression.

NCBI GEO datasets (GSE19650 and GSE43288) were used to investigate the differential transcriptomic signatures of stemness and metabolic genes. The data analysis and processing were performed by quantile normalization and log2 transformation. **A-N**, Representation of the differentially expressed glycolysis genes (A-G), OXPhos genes (H-K), Myc (L), PPARGC1A (M), and CPT2 (N) in indicated samples: normal pancreas (NP) (N=7), intraductal papillary mucinous neoplasm (IPMN)-derived PDAC (IPMN-PDAC) (n=3),

intraductal papillary mucinous adenoma (IPMA) or IPMN with low-grade dysplasia (n=6), intraductal papillary mucinous carcinoma (IPMC) or IPMN with high-grade dysplasia (n=6). **O-X**, Representation of the differentially expressed glycolysis genes (O-U), fatty acid β-oxidation genes (V-W), and PPARGC1A (X) in indicated samples: Normal pancreas (NP) (n=3), pancreatic intraepithelial neoplasia (PanIN) (n=13), and PDAC (n=4). Data represent mean ± SD. p-values were calculated using ordinary one-way ANOVA (multiple comparisons). The mean of each sample was compared with the mean of NP. Asterisks indicate a statistically significant difference between each sample and NP ($p < 0.05$, $^{*}p < 0.05$, $^{**}p < 0.01$, $^{***}p < 0.001$.) **Y**, Venn diagram showing common and unique overexpressed stemness genes in PanIN and IPMN. Data represent mean ± SD. p-values were calculated using ordinary one-way ANOVA (multiple comparisons). ($^{*}p < 0.05$.) **Z**, Network analysis of the differentially expressed stemness and metabolic genes from the GSE19650 dataset using Ingenuity pathway analysis (IPA). The network shows that the PPARGC1A is central to stemness, FAO, and OXPhos pathways in IPMN.

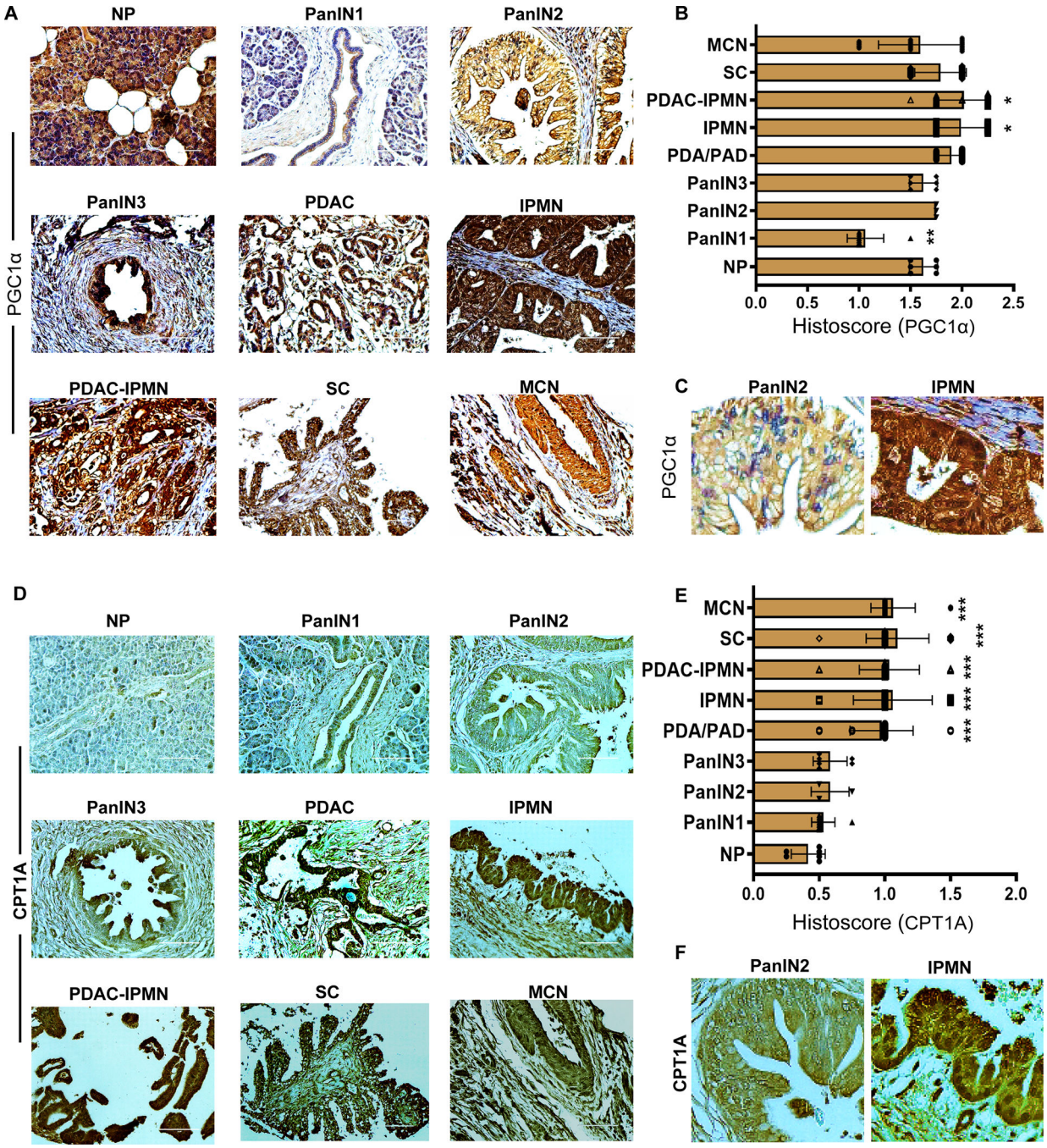

Figure 2. Differential expression of metabolic regulators, PGC1α and CPT1A, in different stages of PDAC development.

A-F, Immunohistochemical analysis of PGC1α (**A-C**) and CPT1A (**D-F**) in indicated samples. A histoscore was calculated by multiplying intensity and positivity. Data represent mean ± SD. P-values were calculated using ordinary one-way ANOVA (multiple comparisons). The mean of each sample was compared with the mean of NP. Asterisks indicate a statistically significant difference between each sample and NP. (*$p < 0.05$, **$p < 0.01$, ***$p < 0.001$.) Scale bar 200 μm. **C and F**, Magnified PanIN2 and IPMN regions

duplicated from the original PanIN2 and IPMN IHC images of Figures 2A and D to show the subcellular localization of PGC1α (C) CPT1A (**F**) were shown.

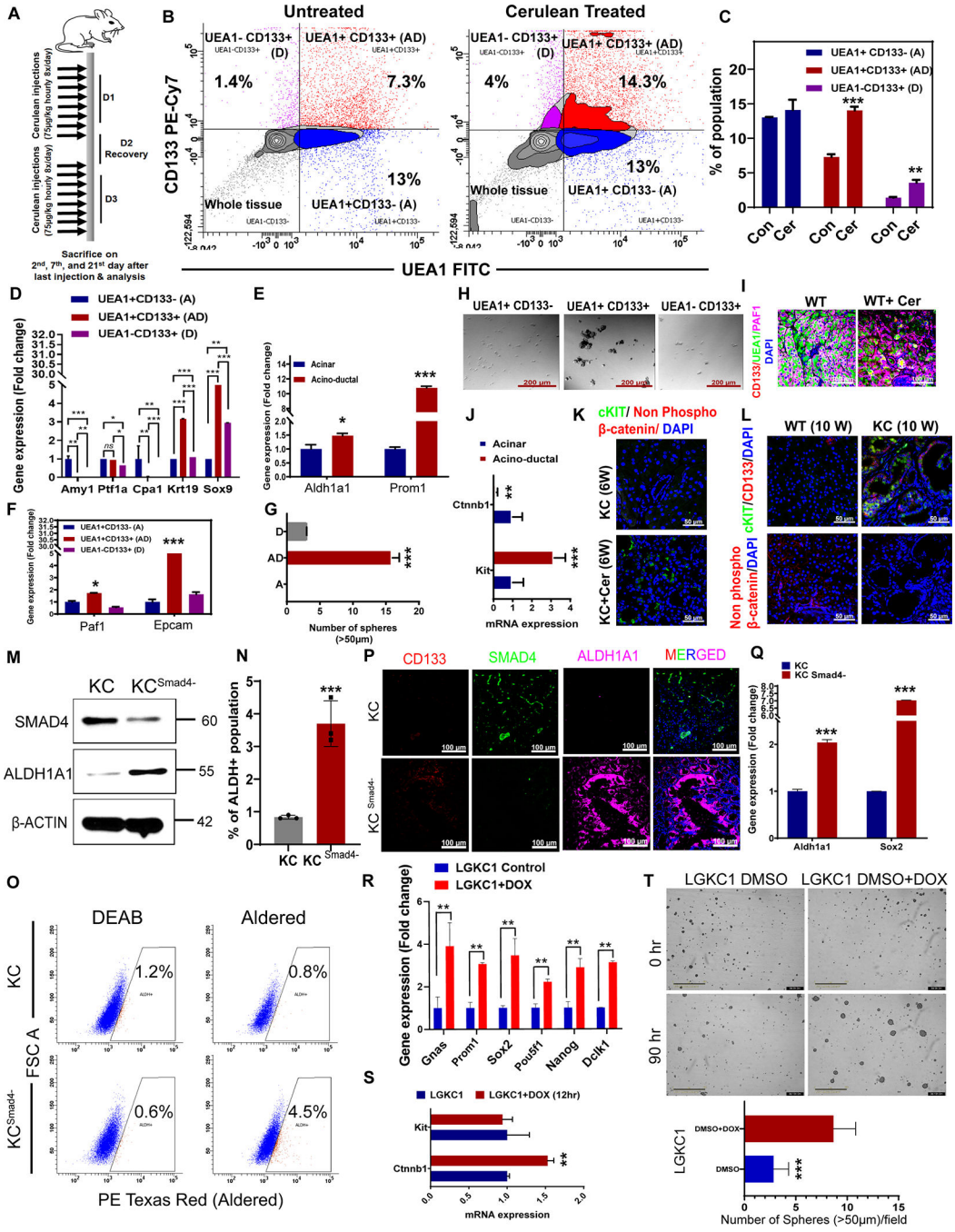

Figure 3. ADM/PanIN and IPMN show stemness features.

A, Schematic depicting the strategy used to develop cerulean-induced mouse model. **B**, Representative flow cytometry plots of acinar, AD, and ductal populations in pancreatic cells isolated from PBS- or cerulean-treated wild-type (WT) mice stained with CD133 PE-Cy7 and UEA1-FITC. **C**, The percentage of AD (UEA1+CD133+), ductal (UEA1-CD133+), and acinar (UEA1+CD133-) populations as analyzed by flow cytometry. **D-F**, Relative expression of indicated genes in acinar, AD, and ductal cells, analyzed by qRT-PCR. The PCR data were normalized with the Actb gene. Data represent mean ± SD (n=3). **G-H,**

Sphere assay in indicated samples. The histogram depicts the number of spheres (>50 μm). Data represent mean ± SD (n=3). **I**, Immunofluorescence images of pancreas harvested from PBS- or cerulean-treated WT mice stained with UEA1-FITC, CD133, PAF1, DAPI (as indicated). Scale bar 100 μm. **J**, Relative expression of indicated genes in acinar and AD cells, analyzed by qRT-PCR. The PCR data were normalized with the Actb gene. Data represent mean ± SD (n=3). (**K-L**), Immunofluorescence images of pancreas harvested from indicated mice stained with c-KIT, non-phospho active β-catenin, CD133, and DAPI (as indicated), Scale bar 50 μm. (**M**), Western blot analysis for proteins indicated on the left using protein lysates from KC6141 (KC) and T161 (KC Smad4^{Loss}). **N-O,** The histogram provides the percentage of ALDH+ cells analyzed by flow cytometry in KC and KC Smad4^{Loss} cells. Representative flow cytometry plots of AldeRed assay for ALDH detection using a combination of Green laser (532 nm) with PE-Texas red detector (615 nm). **P**, Immunofluorescence images of KC and KC Smad4^{Loss} pancreas tissues stained for CD133, Smad4, and DAPI (as indicated), and then examined by confocal microscopy. (Scale bar 100 μm). **Q-S**, Relative gene expression of Aldh1a1, Sox2, Gnas, Prom1, Pou5f1, Nanog, Dclk1 Ctnnb1, and Kit in indicated samples as analyzed by qRT-PCR. The PCR data were normalized with the Actb gene. **T**, Sphere assay images of indicated samples. Scale bar 400 μm. The histogram depicts the number of spheres (>50 μm). For all histograms, data represent mean ± SD (n=6). p-values were calculated by Student's t-test. (*$p < 0.05$, **$p < 0.01$, ***$p < 0.001$.)

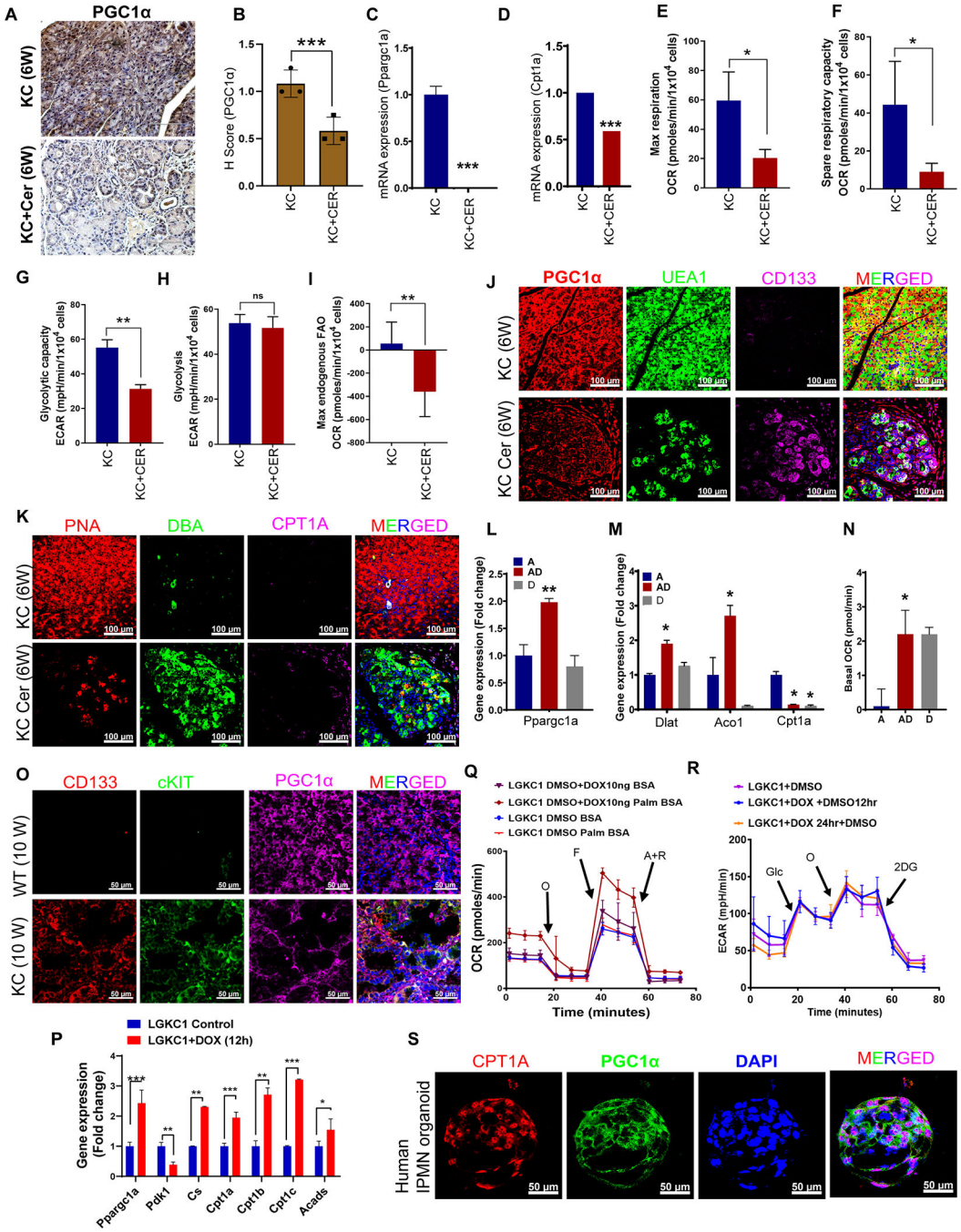

Figure 4. ADM/PanIN and IPMN show upregulation of PGC1α and display unique metabolic states.

A-B, Immunohistochemical analysis of PGC1α in PBS- or cerulean-treated KC pancreas samples. The histogram to the *right* shows the histoscore of PGC1α. Data represent mean ± SD (n=3). Scale bar 200 μm. **C-D**, qRT- PCR analysis of PPARGC1A and CPT1A in indicated samples. The PCR data were normalized with the Actb gene. Data represent mean ± SD (n=3). **E-F**, Maximal respiration and spare respiratory capacity reflected by oxygen consumption rate (OCR) were measured using the Seahorse extracellular flux analyzer. Data

are mean ± S.E.M. (n=6). **G-H**, Glycolysis and glycolytic capacity reflected by extracellular acidification rate (ECAR) was measured in indicated samples using Seahorse extracellular flux analyzer. Data are mean ± S.E.M. (n=6). **I**, Maximal endogenous OCR due to fatty acid oxidation (FAO) measured by XF Palmitate-BSA FAO Substrate with the XF Cell Mito Stress Test kit using the Seahorse extracellular flux analyzer. Data are mean ± S.E.M (n=3). **J-K**, Immunofluorescence images of pancreas harvested from PBS- or cerulean-treated KC mice stained with PNA-Rhodamine, DBA-FITC, UEA1-FITC, CD133, PGC1α, CPT1A, and DAPI (as indicated). Scale bar 100 μm. **L-M**, qRT- PCR analysis of indicated genes in indicated samples. The PCR data were normalized with the Actb gene. Data represent mean ± SD (n=3). **N**, Basal OCR was measured in acinar, AD, and ductal populations using XF Cell Mito Stress Test kit using the Seahorse extracellular flux analyzer. Data are mean ± S.E.M (n=3). **O,** Immunofluorescence images of pancreas harvested from 10-week-old KC and WT mice stained with CD133, PGC1α, cKIT, and DAPI (as indicated). Scale bar 50 μm. **P**, qRT- PCR analysis of indicated genes in LGKC1 control and Dox-induced samples. The PCR data were normalized with the Actb gene. Data represent mean ± SD (n=3). **Q**, OCR was measured following the addition of oligomycin (O) (1 μM), FCCP (F) (0.5 μM), and electron transport inhibitor rotenone/antimycin A (R/A) (0.5 μM). Data are mean ± S.D. (n=6). **R**, ECAR was measured following the addition of glucose (Glc) (10 mM), oligomycin (O) (1 μM), and 2-deoxyglucose (2-DG) (50 mM). Data are mean ± S.E.M. (n=6). **S**, Immunofluorescence images of human IPMN organoids stained with PGC1α, CPT1A, and DAPI (as indicated). Scale bar 50 μm.

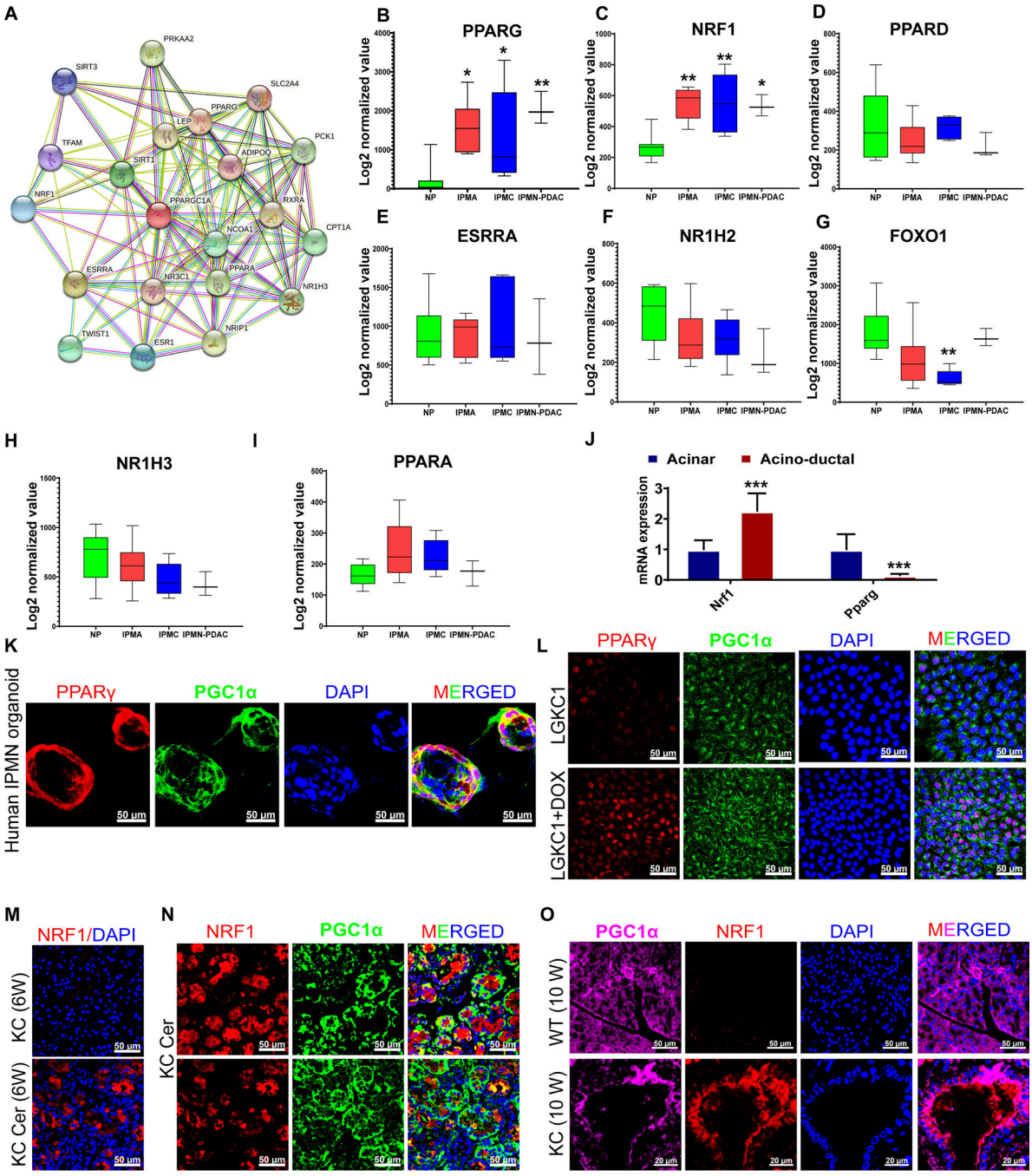

Figure 5. ADM/PanIN and IPMN show the upregulation of unique PGC1α-interacting partners.

A, Protein-protein interactions analysis of PPARGC1A using 'STRING' software. **B-I**, A meta-analysis of genes that encode PGC1α-interacting proteins using the human IPMN progression dataset GSE19650. Datasets were processed using standard GEO2R analysis, followed by quantile normalization and log2 transformation. Data represent mean ± SD. p-values were calculated using ordinary one-way ANOVA (multiple comparisons). The mean of each sample was compared with the mean of NP. Asterisks indicate a statistically significant difference between each sample and NP. **J**, qRT- PCR analysis of indicated genes

in acinar and acino-ductal cells. The PCR data were normalized with the Actb gene. Data represent mean ± SD (n=3). **K-L**, Immunofluorescence images with PGC1α, PPARγ, and DAPI staining on indicated samples. **M-N**, Immunofluorescence images. NRF1 staining along with DAPI on pancreatic tissues harvested from control (KC) and cerulean-treated KC (KC+Cer) mouse (**M**). The KC+Cer immunofluorescence image, which was shown for NRF1 staining in Figure 5M (lower image), was further showed for the co-expression of NRF1 with PGC1α (Figure 5N, **lower images**). The co-expression of NRF1 with PGC1α was shown in another KC+Cer tissue section (Figure 5N, **upper images**). **O**, Immunofluorescence images with PGC1α, NRF1, and DAPI staining on indicated samples. Scale bar 50 μm. For all histograms, p-values were calculated by Student's t-test. (*$p < 0.05$, **$p < 0.01$, ***$p < 0.001$.)

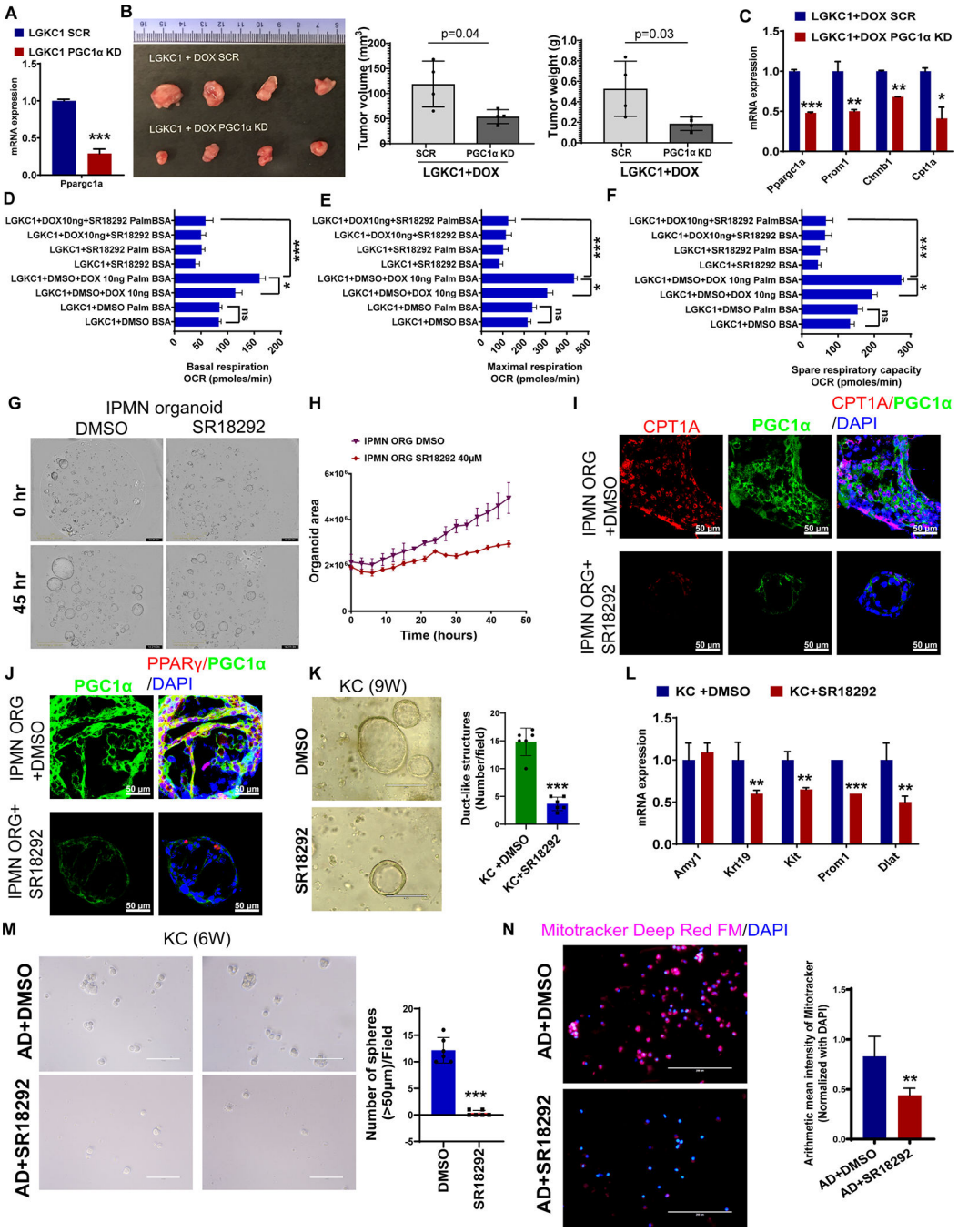

Figure 6. PGC1α-mediated OXPhos and FAO-OXPhos regulate stemness in ADM/PanIN and IPMN, respectively.

A, qRT- PCR analysis of Ppargc1a in the scramble and PGC1α KD in LGKC1 cells. The PCR data were normalized with the Actb gene. Data represent mean ± SD (n=3). **B**, LGKC1 scramble (SCR) and PGC1α KD cells were injected subcutaneously into nude mice and maintained with doxycycline in water. The subcutaneous tumors were excised 21 days after implantation, followed by the measurement of tumor volume and weight (bar graphs). Data are mean ± S.D. (n=4). The significance was determined by a t-test. (*p<0.05, **p<0.01,

$^{***}p<0.001$.) **C**, qRT- PCR analysis of indicated genes in the scramble and PGC1α KD LGKC1+DOX cells. The PCR data were normalized with the Actb gene. Data represent mean ± SD (n=3). **D-F**, Basal, maximal respiration, and spare respiratory capacity reflected by OCR due to fatty acid oxidation (FAO) measured by XF Palmitate-BSA FAO Substrate with the XF Cell Mito Stress Test kit using the Seahorse extracellular flux analyzer. Data are mean ± S.E.M (n=3). **G-H**, Morphology of human IPMN organoids growing in the presence and absence of SR18292. Organoid growth was monitored in the Incucyte Live-Cell Imaging analysis system, which captured images once every 3 hours. Data represent mean ± S.E.M (n=3). **I-J**, Immunofluorescence images of human IPMN organoids stained with PGC1α, PPARγ, CPT1A, and DAPI (as indicated). Scale bar 50 μm. **K**, 3D Matrigel culture of pancreatic cells isolated from 9-week-old KC mouse pancreas and treated with DMSO or SR18292. The bar graph shows the number of duct-like structures per field. Data represent mean ± SD (n=6 fields). **L**, qRT- PCR analysis of indicated genes in DMSO- or SR18292-treated KC pancreatic cells cultured in 3D Matrigel. The PCR data were normalized with the Actb gene. Data represent mean ± SD (n=3). **M**, Sphere assay in AD cells sorted from the pancreatic cells of cerulean-treated KC mice. The AD cells were treated with SR18292 at 40 μM for seven days, followed by sphere count (>50 μm) and imaging analysis. The histogram to the *right* of sphere images depicts the number of spheres(>50 μm) in indicated samples. Data represent mean ± SD (n=4). **N**, Immunofluorescence staining with Mitotracker Deep Red FM and DAPI in SR18292-treated and untreated AD cells sorted from the pancreatic cells of cerulean-treated KC mice. The histogram to the *right* depicts the arithmetic mean intensity of Mitotracker staining normalized with total DAPI staining. Data represent mean ± SD (n=8 random images). For all histograms, p-values were calculated by Student's t-test. ($^{*}p < 0.05$, $^{**}p < 0.01$ $^{***}p < 0.001$.)

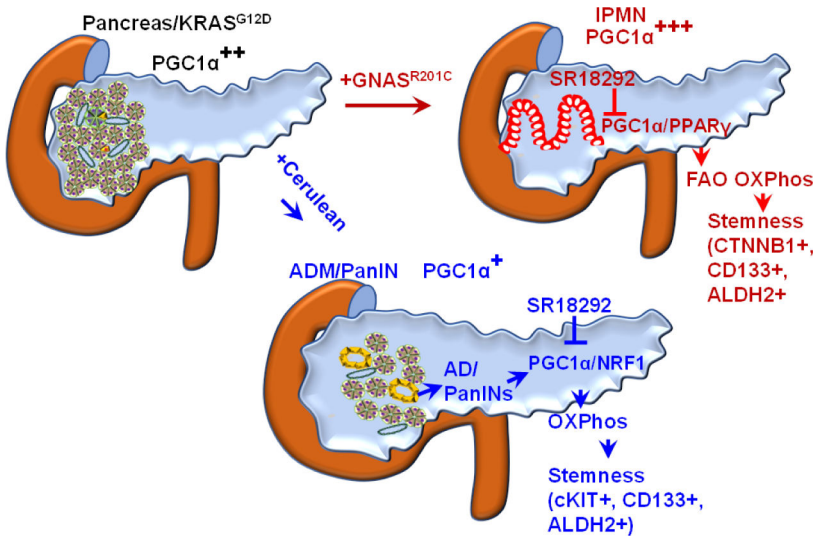

Figure 7.
Schematic diagram depicting the overall findings of the study.